faults. We have demonstrated this phenomenon in a friction-based fault model, but the overall dynamics of the process should be similar for viscoplastic deeper fault extensions, which may dynamically localize and weaken due to shear-heating and strain-rate effects during large earthquakes (*19*) and maintain their localization through the interseismic period because of the resulting structural differences in terms of their grain size and heterogeneity (*31*). Our study has focused on major strike-slip faults, but it has important relevance for the seismic hazard of megathrust subduction zones that are seismically quiescent, such as the Cascadia subduction zone, given the critical effect of down-dip rupture limit on coastal shaking.

REFERENCES AND NOTES

1. C. H. Scholz, *The Mechanics of Earthquakes and Faulting* (Cambridge Univ. Press, New York, ed. 2, 2002).
2. F. M. Chester, J. S. Chester, *Tectonophysics* **295**, 199–221 (1998).
3. D. R. Shelly, *Nature* **463**, 648–652 (2010).
4. R. E. Reilinger *et al.*, *Science* **289**, 1519–1524 (2000).
5. J. Cole *et al.*, *J. Geophys. Res. Solid Earth* **112**, B12304 (2007).
6. F. Waldhauser, W. L. Ellsworth, D. P. Schaff, A. Cole, *Geophys. Res. Lett.* **31**, L18608 (2004).
7. E. Hauksson, W. Yang, P. M. Shearer, *Bull. Seismol. Soc. Am.* **102**, 2239–2244 (2012).
8. N. Lapusta, J. R. Rice, *J. Geophys. Res. Solid Earth* **108**, 2205 (2003).
9. P. M. Mai, K. K. S. Thingbaijam, *Seismol. Res. Lett.* **85**, 1348–1357 (2014).
10. Supplementary materials are available on *Science* Online.
11. Y. Fialko, *Nature* **441**, 968–971 (2006).
12. A. Lin *et al.*, *Tectonophysics* **402**, 21–35 (2005).
13. T. Shimamoto, *J. Struct. Geol.* **11**, 51–64 (1989).
14. B. E. Shaw, S. G. Wesnousky, *Bull. Seismol. Soc. Am.* **98**, 1633–1641 (2008).
15. J. Dieterich, in *Treatise on Geophysics*, G. Schubert, Ed. (Elsevier, Oxford, ed. 2, 2007), vol. 4, pp. 93–110.
16. S. Barbot, N. Lapusta, J.-P. Avouac, *Science* **336**, 707–710 (2012).
17. G. Di Toro *et al*., *Nature* **471**, 494–498 (2011).
18. J. R. Rice, *J. Geophys. Res.* **111**, B05311 (2006).
19. J. D. Platt, J. W. Rudnicki, J. R. Rice, *J. Geophys. Res. Solid Earth* **119**, 4334–4359 (2014).
20. H. Noda, N. Lapusta, *Nature* **493**, 518–521 (2013).
21. R. H. Sibson, *Nature* **243**, 66–68 (1973).
22. P. Segall, A. M. Bradley, *J. Appl. Mech.* **79**, 031013 (2012).
23. G. Hirth, N. M. Beeler, *Geology* **43**, 223–226 (2015).
24. J. C. Savage, *J. Geophys. Res.* **111**, B04405 (2006).
25. M. Bouchon, H. Karabulut, *Science* **320**, 1323–1325 (2008).
26. K. E. Sieh, *Bull. Seismol. Soc. Am.* **68**, 1421–1434 (1978).
27. O. Zielke, J. R. Arrowsmith, L. G. Ludwig, S. O. Akçiz, *Science* **327**, 1119–1122 (2010).
28. B. R. Smith-Konter, D. T. Sandwell, P. M. Shearer, *J. Geophys. Res.* **116**, B06401 (2011).
29. L. B. Grant, A. Donnellan, *Bull. Seismol. Soc. Am.* **84**, 241–246 (1994).
30. E. E. Runnerstrom, L. B. Grant, J. R. Arrowsmith, D. D. Rhodes, E. M. Stone, *Bull. Seismol. Soc. Am.* **92**, 2659–2669 (2002).
31. P. B. Kelemen, G. Hirth, *Nature* **446**, 787–790 (2007).
32. G. C. Beroza, *Bull. Seismol. Soc. Am.* **81**, 1603–1621 (1991).
33. J. L. Elliott, J. T. Freymueller, B. Rabus, *J. Geophys. Res.* **112**, B06421 (2007).

QUANTUM SIMULATION

Quantum spin dynamics and entanglement generation with hundreds of trapped ions

Justin G. Bohnet,[1]* Brian C. Sawyer,[1,2] Joseph W. Britton,[1,3] Michael L. Wall,[4] Ana Maria Rey,[5] Michael Foss-Feig,[3,6] John J. Bollinger[1]*

Quantum simulation of spin models can provide insight into problems that are difficult or impossible to study with classical computers. Trapped ions are an established platform for quantum simulation, but only systems with fewer than 20 ions have demonstrated quantum correlations. We studied quantum spin dynamics arising from an engineered, homogeneous Ising interaction in a two-dimensional array of $^9Be^+$ ions in a Penning trap. We verified entanglement in spin-squeezed states of up to 219 ions, directly observing 4.0 ± 0.9 decibels of spectroscopic enhancement, and observed states with non-Gaussian statistics consistent with oversqueezed states. The good agreement with ab initio theory that includes interactions and decoherence lays the groundwork for simulations of the transverse-field Ising model with variable-range interactions, which are generally intractable with classical methods.

Q uantum simulation, in which a well-controlled quantum system emulates another system to be studied, can be used to address classically intractable problems in fields including condensed-matter and high-energy physics, cosmology, and chemistry (*1–3*). Of particular interest are simulations of the transverse-field Ising spin model (*4*), described by the Hamiltonian

$$\hat{H}_T = \hat{H}_I + \hat{H}_B \qquad (1)$$

$$\hat{H}_I = \frac{1}{N}\sum_{i<j}^{N} J_{i,j}\hat{\sigma}_i^z\hat{\sigma}_j^z, \quad \hat{H}_B = \sum_i^N B_x\hat{\sigma}_i^x \qquad (2)$$

where N is the number of spins, $J_{i,j}$ parameterizes the spin-spin interaction, B_x parameterizes a transverse magnetic field, and $\hat{\sigma}^z$, $\hat{\sigma}^x$ are Pauli spin matrices. A quantum simulation of $\hat{H}_T$ could illuminate complex phenomena in quantum magnetism, including quantum phase transitions, many-body localization, and glassiness in spin systems (*5–8*), and clarify whether quantum annealing can provide an advantage for solving hard optimization problems (*9, 10*).

Ensembles of photons, ions, neutral atoms, molecules, and superconducting circuits are all being developed as quantum simulation platforms (*3*). A variety of quantum spin models have been realized with large ensembles of neutral atoms (*11–15*) and molecules (*16*). Trapped-ion quantum simulators can implement $\hat{H}_T$ (*17–19*) and have a number of advantages over other implementations, such as high-fidelity state preparation and readout, long trapping and coherence times, and strong, variable-range spin-spin couplings. To date, trapped-ion simulators have been constrained to systems of about 20 spins (*18, 20*), for which classical numerical simulations remain tractable; substantial engineering efforts are under way to increase the number of ions by cryogenically cooling linear traps and two-dimensional (2D) surface-electrode traps (*21, 22*).

Penning traps have emerged as a viable option for performing quantum simulations with hundreds of ions (*23–26*). Laser-cooled ions in a Penning trap self-assemble into 2D triangular lattices and are amenable to similar high-fidelity spin-state control, long trapping times, and generation of transverse-field Ising interactions as ions in linear Paul traps. Previous work in Penning traps demonstrated control of the collective spin (*27*) and benchmarked the engineered, variable-range Ising interaction in the mean-field, semiclassical limit (*24–26*). However, for a simulator of quantum magnetism to be trusted, quantum

[1]National Institute of Standards and Technology (NIST), Boulder, CO 80305, USA. [2]Georgia Tech Research Institute, Atlanta, GA 30332, USA. [3]Army Research Lab, Adelphi, MD 20783, USA. [4]JILA, NIST, and University of Colorado, Boulder, CO 80309, USA. [5]JILA, NIST, and Department of Physics, University of Colorado, Boulder, CO 80309, USA. [6]Joint Quantum Institute and NIST, Gaithersburg, MD 20899, USA.
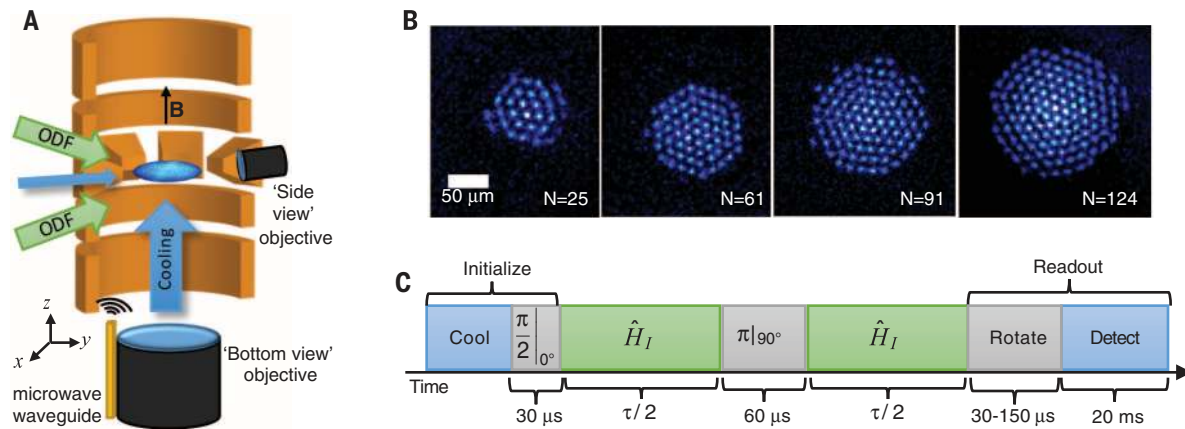*Corresponding author. Email: justin.bohnet@nist.gov (J.G.B.); jjb@nist.gov (J.J.B.)

Fig. 1. Penning trap quantum simulator. (**A**) A cross-sectional illustration of the Penning trap (not to scale). The orange electrodes provide axial confinement and the rotating wall potential. The 4.5 T magnetic field is directed along the z axis. The blue disk indicates the 2D ion crystal. Resonant Doppler cooling is performed with the beams along z and y. The spin state–dependent optical dipole force (ODF) beams enter ±10° from the 2D ion plane. Resonant microwave radiation for coupling ground states |↑⟩ and |↓⟩ is delivered through a waveguide. State-dependent fluorescence is collected through the pair of imaging objectives, where the bright state corresponds to |↑⟩. (**B**) Coulomb crystal images in a frame rotating at ω_r with ^{9}Be$^+$ ions in |↑⟩, with the number of ions N indicated. (**C**) The typical experiment pulse sequence, composed of cooling laser pulses (blue), microwave pulses (gray), and ODF laser pulses (green). Cooling and repumping initialize each ion in |↑⟩, and then a microwave π/2 pulse prepares the spins along the x axis. Suddenly switching on $\hat{H}_I$ initiates the non-equilibrium spin dynamics. The microwave π pulse implements a spin echo, reducing dephasing from magnetic field fluctuations and ODF laser light shifts. State readout consists of a final global rotation and fluorescence detection. The final microwave pulse area and phase are chosen to measure the desired spin projection.
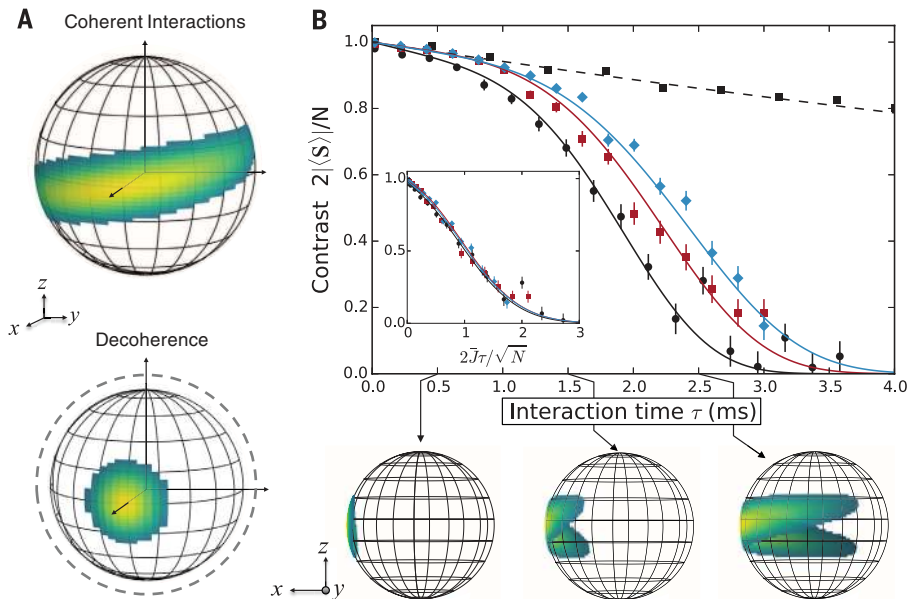

Fig. 2. Depolarization of the collective spin from spin-spin interactions and decoherence. (**A**) The Husimi distribution of the collective spin state on a Bloch sphere calculated for the experimental parameters in (B), with N = 21, illustrating (top) an oversqueezed state generated by the Ising interaction at time τ = 2 ms with no decoherence and (bottom) a loss of contrast only from decoherence, effectively shrinking the Bloch sphere. (**B**) Contrast versus interaction time for N = 21, 58, and 144 ions indicated by black circles, red squares, and blue diamonds, respectively. Data are means ± SD; the solid lines are predictions, with no free parameters, from a model that includes decoherence from spontaneous emission (28). The contrast decay from decoherence caused by spontaneous emission is measured in the absence of spin-spin coupling (black squares with the dashed line showing an exponential fit). At each τ, the detuning δ is adjusted to eliminate spin-motion coupling at the end of the experiment, resulting in a different $\bar{J} \propto 1/\delta$ for each point. The Bloch spheres show the Husimi distribution for a pure state of N = 21 at three different interaction times, ignoring the effects of decoherence. Inset: The data collapse to a common curve with proper rescaling, indicating that the depolarization is dominated by coherent spin-spin interactions.

correlations generated by the Ising interaction must be observed and understood. For large trapped-ion simulators, this benchmarking requires a detailed accounting of many-body physics in an open quantum system.

Here, we observed and benchmarked entanglement in hundreds of trapped ions generated with engineered Ising interactions in a 2D array of ^{9}Be$^+$ ions in a Penning trap. To enable efficient theoretical computation of the spin dynamics (28), we performed experiments with a homogeneous Ising interaction and without simultaneous application of the transverse field B_x, finding good agreement with a solution of the full quantum master equation.

Our experimental system consists of between 20 and 300 ^{9}Be$^+$ ions confined to a single-plane Coulomb crystal in a Penning trap (Fig. 1) (28). The trap is characterized by an axial magnetic field |**B**| = 4.45 T and an axial trap frequency $\omega_z = 2\pi \times$ 1.57 MHz. A stack of cylindrical electrodes generates a harmonic confining potential along their axis. Radial confinement is provided by the Lorentz force from **E** × **B**–induced rotation in the axial magnetic field. Time varying potentials applied to eight azimuthally segmented electrodes generate a rotating wall potential that controls the crystal rotation frequency ω_r, typically between $2\pi \times 172$ kHz and $2\pi \times 190$ kHz.

The spin-½ system is the $^2S_{1/2}$ ground state of the valence electron spin |↑⟩ ≡ $|m_s\rangle = +^1/_2$, |↓⟩ ≡ $|m_s\rangle = -^1/_2$. In the magnetic field of the Penning trap, the ground state is split by 124 GHz. A resonant microwave source provides an effective transverse field, which we use to perform global rotations of the spin ensemble with a Rabi frequency of 8.3 kHz. The T_2 spin echo coherence
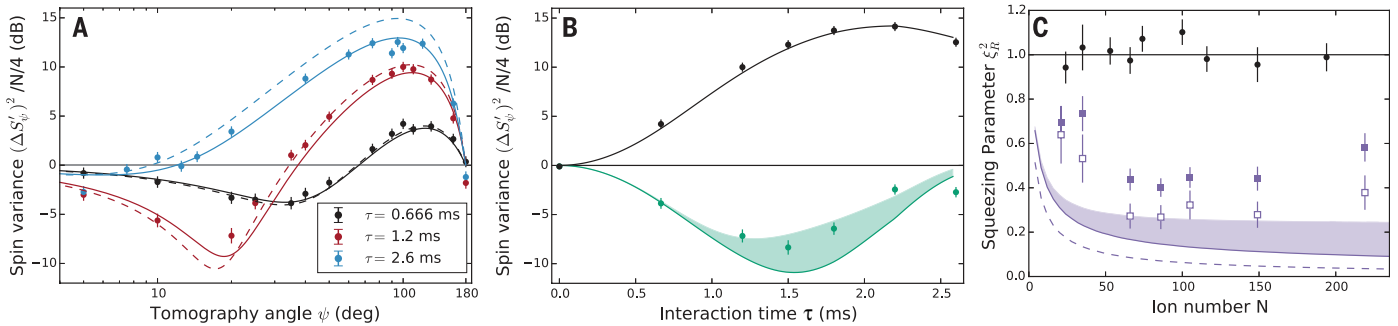
Fig. 3. Spin variance and entanglement. (**A**) Spin variance (symbols) as a function of tomography angle ψ for $N = 86 \pm 2$. The variance is calculated from 200 trials. The solid lines are a prediction, with no free parameters, assuming homogeneous Ising interactions and including decoherence from spontaneous emission (28). The dashed lines are theoretical predictions with the same interaction parameters but no decoherence. (**B**) The explicit time dependence of the spin variance for the ensemble in (A). The data for the minimum (green points) and maximum (black points) spin variance are shown with theory predictions of the optimal squeezing and antisqueezing (solid lines), including decoherence. Because our measurement of $(\Delta S'_\psi)^2$ has substantial granularity, we visualize the effect of finite sampling of ψ on the measured minimum variance using the green shaded region bounded by $\max\{[\Delta S'_\psi(\psi_m \pm 5°)]^2\}$, where ψ_m corresponds to the angle that minimizes $(\Delta S'_\psi)^2$. The ±5° uncertainty does not have a visible effect in the squeezed component for short times, or for the antisqueezing component at any time. (**C**) Ramsey squeezing parameter measured for different ensemble sizes N. The black points show data for the initial unentangled spin state. The solid purple squares show the lowest directly measured ξ_R^2 with no corrections or subtractions of any detection noise for evaluation of the entanglement witness. The open squares show ξ_R^2 inferred by subtracting photon shot noise. The dashed line is the predicted optimal ξ_R^2 from coherent Ising interactions with no decoherence, and the solid line shows the limit including spontaneous emission assuming $\Gamma/\bar{J} = 0.05$, which is typical for our system. The shaded purple region accounts for finite sampling of ψ as in (B). All error bars denote SE.

time is 15 ms. Optical transitions to the $^2P_{3/2}$ states are used for state preparation, Doppler cooling, and projective measurement (28).

The Ising interaction is implemented by a spin-dependent optical dipole force (ODF) generated from the interference of a pair of detuned lasers (Fig. 1A). The ODF couples the spin and motional degrees of freedom through the interaction

$$\hat{H}_{\text{ODF}} = \sum_{i=1}^{N} F_0 \cos(\mu t) \hat{z}_i \hat{\sigma}_i^z \qquad (3)$$

where $\hat{z}_i$ is the position operator for ion i, $\mu/2\pi$ is the ODF laser beat frequency, and F_0 is the force amplitude, typically 30 yN. The ODF drives the axial drumhead modes of the planar ion crystal (25, 26), generating an effective spin-spin interaction by modifying the ions' Coulomb potential energy (29). Detuning μ from ω_z changes the effective range of the spin-spin interaction $J_{i,j} \propto d_{i,j}^{-a}$, where d_{ij} is the ion separation. Although a can range from 0 to 3 (24), in this work we primarily drive the highest-frequency, center-of-mass (COM) mode at ω_z with ODF detunings $\delta = \mu - \omega_z$ ranging from about $2\pi \times 0.5$ kHz to $2\pi \times 3$ kHz, such that a varies from 0.02 to 0.18, respectively. The next closest axial motional mode frequency is more than $2\pi \times 20$ kHz lower than ω_z. Because $a \ll 1$, the Ising interaction is approximately independent of distance, resulting in a homogeneous pairwise coupling $J_{i,j} \approx \bar{J} = F_0^2/(4M\omega_z\delta)$, where M is the ion mass.

At the mean-field level, each spin precesses in an effective magnetic field determined by the couplings to other spins, described by the Hamiltonian

$$\hat{H}_{\text{MF}} = \sum_{j=1}^{N} \frac{\overline{B_j} \hat{\sigma}_j^z}{2} \qquad (4)$$

where

$$\bar{B}_j = \frac{2}{N} \sum_{i \neq j} J_{i,j} \langle \hat{\sigma}_i^z \rangle \qquad (5)$$

We calibrated $\bar{J}$ through measurements of mean-field spin precession (24, 28), typically finding $\bar{J}/h \leq 3300$ s^{-1}. For the experiments described below, we started with all the spins initialized in an eigenstate of $\hat{\sigma}^x$ so that $\bar{B}_j = 0$. This choice of initial condition ensured that the observed physics are dominated by quantum correlations and decoherence alone.

State readout was performed using fluorescence from the Doppler cooling laser on the cycling transition (28). Ions in $|\uparrow\rangle$ fluoresce and ions in $|\downarrow\rangle$ are dark. Global fluorescence was collected with the side-view objective (Fig. 1A) and counted with a photomultiplier tube. We used the bottom-view image to count the number of ions and thereby calibrate the photon counts per ion (Fig. 1B). From the detected photon number, we could infer the bright-state population $N_\uparrow$, which is equivalent to a projective measurement of $\hat{S}_z = \hat{N}_\uparrow - (N/2)$, where $\hat{S}_z$ is the z component of the collective spin vector

$$\mathbf{S} = \frac{1}{2} \sum_i^N (\hat{\sigma}_i^x, \hat{\sigma}_i^y, \hat{\sigma}_i^z) \qquad (6)$$

By performing a final global rotation before measuring, we could measure the moments of any component of **S**. The directly observed variance of the measurement $(\Delta S_z)^2$ is well described by the sum of two noise terms: spin noise $(\Delta S'_z)^2$ and photon shot noise $(\Delta S_{\text{psn}})^2$. Here, ΔX indicates the standard deviation of repeated measurements of $\hat{X}$. In this paper, we use the underlying spin noise $(\Delta S'_z)^2 = (\Delta S_z)^2 - (\Delta S_{\text{psn}})^2$ for comparison with theory predictions, but use the directly

observed variance in the measurement $(\Delta S_z)^2$ for evaluating the spin-squeezing entanglement witness. The ratio $(\Delta S_{\text{psn}})^2/(\Delta S'_z)^2$ is typically 0.13 (−8.8 dB), so the noise subtraction is small for all but the most squeezed states observed here. Other sources of state readout noise are not appreciable (28).

The depolarization of the collective spin length $|\langle \mathbf{S} \rangle|$, or contrast, caused by the Ising interaction is a canonical example of non-equilibrium quantum dynamics (30–33). Quantum correlations reduce the contrast and cause the collective spin state to wrap around the Bloch sphere that represents the state space (Fig. 2A). However, the contrast also decreases from decoherence, which destroys correlations, effectively shrinking the Bloch sphere. Our calculation accounts for both effects; for homogeneous Ising interactions $J_{i,j} = \bar{J}$ and at the time scales explored experimentally, the contrast is approximately (28) given by

$$|\mathbf{S}| \approx \exp(-\Gamma\tau) \frac{N}{2} \left[\cos\left(\frac{2\bar{J}}{N} \tau \right) \right]^{N-1} \qquad (7)$$

where τ is the total ODF interaction time (Fig. 1C) and Γ is the total single-particle decoherence rate (28) due to spontaneous emission from the ODF lasers.

We show the depolarization dynamics of $|\langle \mathbf{S} \rangle|$ in our experiment in Fig. 2B, distinguishing effects of coherent interactions from decoherence. We determined $|\langle \mathbf{S} \rangle|$ from measurements of $\langle \hat{S}_x \rangle$, performing independent experiments to confirm that $\langle \hat{S}_y \rangle = \langle \hat{S}_z \rangle = 0$ after evolution under $\hat{H}_I$. To distinguish the depolarization caused only by decoherence associated with the ODF lasers, we performed experiments at $\delta = +2\pi \times 50$ kHz, effectively eliminating the Ising coupling while leaving the spontaneous emission rate unchanged. The dashed line in Fig. 2B is a fit to the observed

Fig. 4. Full counting statistics of a non-Gaussian spin state and theoretical Fisher information. (**A** and **B**) Histograms showing the squeezed (A) and antisqueezed (B) quadratures of the collective spin of $N = 127 \pm 4$ ions, corresponding to $\psi = 5.4°$ and $\psi = 92°$, respectively; $\tau = 3$ ms. The integral of the histogram is normalized to unity. The red line is the Gaussian distribution of the initial, unsqueezed state. The solid black line is the probability density predicted from numerical calculations (28), assuming homogeneous interactions and including decoherence from spontaneous emission and magnetic field fluctuations. We account for photon shot noise by convolving the theoretical probability density with a Gaussian distribution with a variance $(\Delta S_{psn})^2/(N/4)$.

(**C**) Extraction of the Fisher information from the theoretically computed Hellinger distance without (black) and with (blue) photon shot noise, including the effects of decoherence from spontaneous emission and magnetic field noise. Shown in red is the Hellinger distance in the absence of decoherence or photon shot noise, for comparison. The points denote computed values of the Hellinger distance; the lines are small-angle quartic fits. The gray swath denotes the region of entangled states (28).
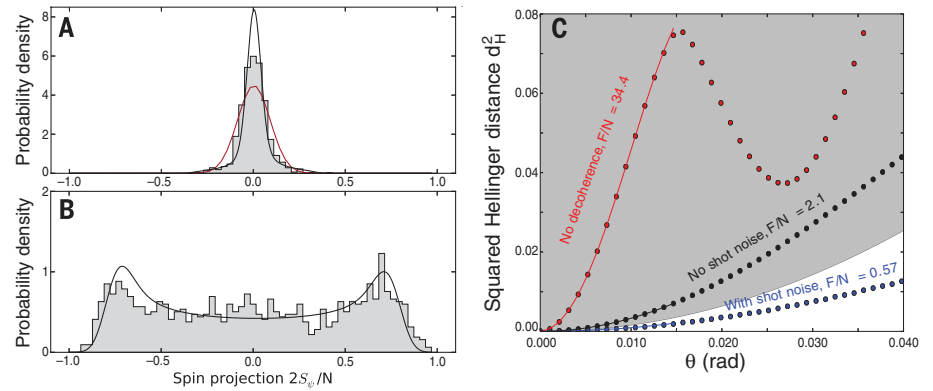
exponential decay, measuring Γ in our system (28). The faster contrast decay for μ tuned near ω_z is in good agreement with Eq. 7 for a range of system sizes. For these data, $\delta = 4\pi/\tau$, ensuring spin-motion decoupling of the COM mode at the end of the experiment (25). The collapse of the data to a single curve when plotted as a function of $2\bar{J}\tau/\sqrt{N}$ (Fig. 2B, inset) provides strong evidence that the depolarization is primarily the result of spin-spin interactions. However, depolarization dynamics alone are not enough to prove that entanglement exists in the ensemble.

To verify entanglement, we used the Ramsey squeezing parameter ξ_R^2, which only requires measuring the variance of collective observables, instead of full state tomography. The Ramsey squeezing parameter is

$$\xi_R^2 = N \frac{\min_\psi[(\Delta S_\psi)^2]}{|\langle S \rangle|^2} \qquad (8)$$

where

$$\hat{S}_\psi = \frac{1}{2} \sum_i^N \cos(\psi) \hat{\sigma}_i^z + \sin(\psi) \hat{\sigma}_i^y \qquad (9)$$

and $\min_\psi$ indicates taking the minimum as a function of ψ. For an unentangled spin state, polarized along the x axis, $|\langle S \rangle| = N/2$ and the spin noise is set by Heisenberg uncertainty relations to $(\Delta S_y)^2 = (\Delta S_z)^2 = N/4$, so $\xi_R^2 = 1$. This quantum noise limits the signal-to-noise ratio for a wide range of quantum sensors based on ensembles of independent quantum objects (34). Nonclassical correlations can redistribute quantum noise between two orthogonal quadratures of the collective spin, squeezing the noise such that $(\Delta S_\psi)^2 < N/4$ and $\xi_R^2 < 1$. These squeezed states are entangled (35), and furthermore, $\xi_R^2 < 1$ proves that the entangled state is a useful resource for precision sensing (15, 34–43).

At short times, the non-equilibrium spin dynamics caused by the Ising interaction can produce spin-squeezed states (15, 32, 34, 44). Figure 3, A and B, shows the measured time evolution of the spin variance $(\Delta S'_\psi)^2$ of 86 ions, normalized to the spin variance of the initial, unentangled

state. We compared the data to an analytic model (32) that assumes homogeneous Ising interactions and fully accounts for both elastic and spin-changing spontaneous emission. The data clearly show the development of squeezed and anti-squeezed quadratures, and deviations from perfectly coherent Ising dynamics are well described by the effects of spontaneous emission alone. Similar data for different values of N are shown in (28).

Using measurements of the directly observed spin variance $(\Delta S_\psi)^2$ and contrast $|\langle S \rangle|$, we obtained ξ_R^2 for a range of values of τ. As shown by a plot of the minimum observed ξ_R^2 for each N in Fig. 3C, the entanglement witness $\xi_R^2 < 1$ is satisfied for seven independent data sets with N ranging from 21 to 219. We observe a minimum $\xi_R^2 = -4.0 \pm 0.9$ dB for $N = 84$ ions. We also show ξ_R^2 measured for the initial state, confirming our calibration of N. For comparison, Fig. 3C shows the absolute minimum ξ_R^2 predicted for coherent Ising interactions. The majority of the observed discrepancy for ensembles ranging from 60 to 150 ions is accounted for by photon shot noise, spontaneous emission, and the finite sampling of τ and ψ. For other ion numbers (28), we still observe good agreement in the antisqueezed spin variance, but the minimum spin variance and ξ_R^2 deviate further from the prediction. We attribute the deviation to technical noise sources (28).

The Ramsey squeezing parameter is an effective entanglement witness at short times when quantum noise is approximately Gaussian. At longer times, the growth of spin correlations causes both the depolarization seen in Fig. 2 and the increase in $\min_\psi[(\Delta S_\psi)^2]$, due to the appearance of non-Gaussian quantum noise in the collective spin. Both effects cause ξ_R^2 to increase above 1, which we call an oversqueezed state. Oversqueezed states can be entangled (45); however, ξ_R^2 can also increase simply because of decoherence.

Signatures of quantum correlations at longer interaction times are seen in a histogram of the measurements of $\langle \hat{S}_\psi \rangle$ for an oversqueezed state

of 127 ions after an interaction time of $\tau = 3$ ms (Fig. 4B). For times well beyond the optimum squeezing time, we see a clear non-Gaussian distribution for the antisqueezed quadrature. The distribution for $\psi = 5.4°$ (Fig. 4A) also contains non-Gaussian characteristics in the tails away from the narrow central feature. We found good agreement between these data and a theoretical model of the full counting statistics. Even though $\xi_R^2 = 26$, the theoretically predicted state is entangled, as shown by an entanglement witness based on the Fisher information F (Fig. 4C). The quantum Fisher information has been used as an entanglement witness in other trapped-ion simulators (46). Here, we bound the value of F using the approach in (40) and find $F/N > 2.1$, which satisfies the inequality of the entanglement witness $F/N > 1$ (45). Photon shot noise in our measurement limits our capability to directly witness the entanglement experimentally (28), but the good agreement with theory indicates that the state of the ensemble is consistent with an entangled, oversqueezed state. Additionally, we experimentally confirmed that this procedure for bounding F witnesses entanglement of squeezed states (fig. S11). The full counting statistics are only efficiently computable for homogeneous couplings, a good approximation for the small detunings δ considered here. For future work with inhomogeneous Ising coupling, obtaining the full counting statistics theoretically will likely be intractable for more than 20 to 30 spins.

The techniques presented here are applicable to precision sensors using trapped ions, where the number of ions is limited by systematic errors arising from ion motion (47), and could be useful for quantum-enhanced metrology with non-Gaussian spin states (40, 48–50). These results benchmark controlled quantum evolution in a 2D platform with more than 200 spins, establishing a foundation for future experiments studying the full transverse-field Ising model in regimes inaccessible to classical computation. With the implementation of single-spin readout, the simulator could provide unique opportunities to study the dynamics of spin correlations in 2D systems,

such as Lieb-Robinson bounds (19) and many-body localization in the presence of disorder (5, 6).

REFERENCES AND NOTES

1. R. P. Feynman, *Int. J. Theor. Phys.* **21**, 467–488 (1982).
2. P. Hauke, F. M. Cucchietti, L. Tagliacozzo, I. Deutsch, M. Lewenstein, *Rep. Prog. Phys.* **75**, 082401 (2012).
3. I. M. Georgescu, S. Ashhab, F. Nori, *Rev. Mod. Phys.* **86**, 153–185 (2014).
4. R. J. Elliott, P. Pfeuty, C. Wood, *Phys. Rev. Lett.* **25**, 443–446 (1970).
5. K. Binder, A. P. Young, *Rev. Mod. Phys.* **58**, 801–976 (1986).
6. R. Nandkishore, D. A. Huse, *Annu. Rev. Condens. Matter Phys.* **6**, 15–38 (2015).
7. D. Belitz, T. R. Kirkpatrick, T. Vojta, *Rev. Mod. Phys.* **77**, 579–632 (2005).
8. S. Sachdev, *Quantum Phase Transitions* (Wiley, 2007).
9. T. F. Rønnow et al., *Science* **345**, 420–424 (2014).
10. A. Lucas, *Front. Phys.* **2**, 5 (2014).
11. J. Simon et al., *Nature* **472**, 307–312 (2011).
12. A. de Paz et al., *Phys. Rev. Lett.* **111**, 185305 (2013).
13. T. Fukuhara et al., *Phys. Rev. Lett.* **115**, 035302 (2015).
14. R. C. Brown et al., *Science* **348**, 540–544 (2015).
15. I. D. Leroux, M. H. Schleier-Smith, V. Vuletić, *Phys. Rev. Lett.* **104**, 073602 (2010).
16. B. Yan et al., *Nature* **501**, 521–525 (2013).
17. D. Porras, J. I. Cirac, *Phys. Rev. Lett.* **92**, 207901 (2004).
18. P. Jurcevic et al., *Nature* **511**, 202–205 (2014).
19. P. Richerme et al., *Nature* **511**, 198–201 (2014).
20. R. Islam et al., *Science* **340**, 583–587 (2013).
21. R. Schmied, J. H. Wesenberg, D. Leibfried, *Phys. Rev. Lett.* **102**, 233002 (2009).
22. C. D. Bruzewicz, R. McConnell, J. Chiaverini, J. M. Sage, http://arxiv.org/abs/1511.03293 (2015).
23. J. D. Baltrusch, A. Negretti, J. M. Taylor, T. Calarco, *Phys. Rev. A* **83**, 042319 (2011).
24. J. W. Britton et al., *Nature* **484**, 489–492 (2012).
25. B. C. Sawyer et al., *Phys. Rev. Lett.* **108**, 213003 (2012).
26. C.-C. J. Wang, A. C. Keith, J. K. Freericks, *Phys. Rev. A* **87**, 013604 (2013).
27. M. J. Biercuk et al., *Quantum Inf. Comput.* **9**, 920–949 (2009).
28. See supplementary materials on *Science* Online.
29. D. Leibfried et al., *Nature* **422**, 412–415 (2003).
30. M. Kastner, *Phys. Rev. Lett.* **106**, 130601 (2011).
31. M. V. D. Worm, B. C. Sawyer, J. J. Bollinger, M. Kastner, *New J. Phys.* **15**, 083007 (2013).
32. M. Foss-Feig, K. R. A. Hazzard, J. J. Bollinger, A. M. Rey, *Phys. Rev. A* **87**, 042101 (2013).
33. K. R. A. Hazzard et al., *Phys. Rev. A* **90**, 063622 (2014).
34. D. Wineland, J. Bollinger, W. Itano, F. Moore, D. J. Heinzen, *Phys. Rev. A* **46**, R6797 (1992).
35. A. Sørensen, L. M. Duan, J. I. Cirac, P. Zoller, *Nature* **409**, 63–66 (2001).
36. L. K. Shalm, R. B. A. Adamson, A. M. Steinberg, *Nature* **457**, 67–70 (2009).
37. W. Wasilewski et al., *Phys. Rev. Lett.* **104**, 133601 (2010).
38. C. D. Hamley, C. S. Gerving, T. M. Hoang, E. M. Bookjans, M. S. Chapman, *Nat. Phys.* **8**, 305–308 (2012).
39. C. F. Ockeloen, R. Schmied, M. F. Riedel, P. Treutlein, *Phys. Rev. Lett.* **111**, 143001 (2013).
40. H. Strobel et al., *Science* **345**, 424–427 (2014).
41. N. Behbood et al., *Phys. Rev. Lett.* **113**, 093601 (2014).
42. O. Hosten, N. J. Engelsen, R. Krishnakumar, M. A. Kasevich, *Nature* **529**, 505–508 (2016).
43. K. C. Cox, G. P. Greve, J. M. Weiner, J. K. Thompson, *Phys. Rev. Lett.* **116**, 093602 (2016).
44. M. Kitagawa, M. Ueda, *Phys. Rev. A* **47**, 5138–5143 (1993).
45. L. Pezzé, A. Smerzi, *Phys. Rev. Lett.* **102**, 100401 (2009).
46. J. Smith et al., http://arxiv.org/abs/1508.07026 (2015).
47. K. Arnold et al., *Phys. Rev. A* **92**, 032108 (2015).
48. B. Lücke et al., *Phys. Rev. Lett.* **112**, 155304 (2014).
49. F. Haas, J. Volz, R. Gehr, J. Reichel, J. Estève, *Science* **344**, 180–183 (2014).
50. R. McConnell, H. Zhang, J. Hu, S. Ćuk, V. Vuletić, *Nature* **519**, 439–442 (2015).

OPTICAL MATERIALS

A highly efficient directional molecular white-light emitter driven by a continuous-wave laser diode

Nils W. Rosemann,[1,2] Jens P. Eußner,[2,3] Andreas Beyer,[1,2] Stephan W. Koch,[1,2] Kerstin Volz,[1,2] Stefanie Dehnen,[2,3]* Sangam Chatterjee[1,2,4]*

Tailored light sources have greatly advanced technological and scientific progress by optimizing the emission spectrum or color and the emission characteristics. We demonstrate an efficient spectrally broadband and highly directional warm-white-light emitter based on a nonlinear process driven by a cheap, low-power continuous-wave infrared laser diode. The nonlinear medium is a specially designed amorphous material composed of symmetry-free, diamondoid-like cluster molecules that are readily obtained from ubiquitous resources. The visible part of the spectrum resembles the color of a tungsten-halogen lamp at 2900 kelvin while retaining the superior beam divergence of the driving laser. This approach of functionalizing energy-efficient state-of-the-art semiconductor lasers enables a technology complementary to light-emitting diodes for replacing incandescent white-light emitters in high-brilliance applications.

The impact of well-managed light on our everyday life is immeasurable (1, 2). The light-emitting diode (LED) is one of the most prominent developments since the invention of incandescent lightbulbs in the late 1800s (3). The latter dissipate most energy in the infrared as heat, whereas typical white LEDs cover only the visible spectrum. Most prominent examples of white-light LEDs are based on gallium nitride (4, 5). Their narrow-band ultraviolet (UV) emission is converted into visible light by applying phosphors (6–9). This cold light has tremendous advantages with respect to energy efficiency. Other concepts pursued for efficient white-light generation include the combination of red, green, and blue emitters (10), which is currently the path of choice for organic LEDs (11–14). All types of LEDs excel due to their virtually Lambertian emission patterns that are highly desirable for applications like active displays that require large viewing angles (15). However, this poses challenges in targeted illumination and projection of light due to the associated large etendue $G = A\Omega$, where A is the source area and Ω is the solid angle of emission (16). Ideally, the etendue remains constant throughout an entire optical system where light undergoes perfect reflections or refractions. It can increase—for example, when impinging on a diffusor—but cannot be decreased without loss in radiance. This renders low-etendue sources extremely desirable for devices requiring high spatial resolution like microscopes or for applications with high throughput, such as projection systems.

Other concepts of white-light generation by monochromatic sources besides phosphors rely on nonlinear effects that provide very broadband supercontinua and are widely used in many scientific applications (17, 18). These are often referred to as brilliant sources. They generally feature small, point-source–like emission areas due to the tightly focused short-pulsed driving lasers that are used to overcome the vast peak electric field strength required to invoke the extremely nonlinear effects such as soliton formation (19). Hence, the related challenges, such as the system size, price, and energy requirements, restrict the use of supercontinuum sources to scientific laboratory use and the medical sector—for example, in coherent anti–Stokes Raman scattering (20) or optical coherence tomography (21), as well as for defense and security applications.

Here, we use a molecule-based solid compound as an extremely nonlinear medium. It enables the steady-state operation of a low-etendue, directional broadband white-light source covering the entire

[1]Fachbereich Physik, Philipps-Universität Marburg, DE-35032 Marburg, Germany. [2]Wissenschaftliches Zentrum für Materialwissenschaften, Philipps-Universität Marburg, DE-35032 Marburg, Germany. [3]Fachbereich Chemie, Philipps-Universität Marburg, DE-35032 Marburg, Germany. [4]Institute of Experimental Physics I, Justus-Liebig-University, DE-35392 Giessen, Germany.
*Corresponding author. Email: stefanie.dehnen@uni-marburg.de (S.D.); sangam.chatterjee@physik.uni-giessen.de (S.C.)

Supplementary Materials for

Quantum spin dynamics and entanglement generation with hundreds of trapped ions

Justin G. Bohnet,* Brian C. Sawyer, Joseph W. Britton, Michael L. Wall, Ana Maria Rey, Michael Foss-Feig, John J. Bollinger*

*Corresponding author. Email: justin.bohnet@nist.gov (J.G.B.); jjb@nist.gov (J.J.B.)

This PDF file includes:

Materials and Methods

Figs. S1 to S11

References

Materials and Methods

$^9\text{Be}^+$ Spin-1/2, Control, and Detection

Reference (*27*) and the supplementary material to (*24*) give detailed descriptions of our spin initialization, control, and measurement capabilities with planar ion arrays in Penning traps. We briefly summarize some of that discussion, emphasizing aspects relevant for the measurements reported here. Figure S1 shows the relevant $^9\text{Be}^+$ energy levels. We use the valence electron spin states parallel $|\uparrow\rangle = \left|m_J = +\frac{1}{2}\right\rangle$ and anti-parallel $|\downarrow\rangle = \left|m_J = -\frac{1}{2}\right\rangle$ to the applied magnetic field of the Penning trap as the spin-$1/2$ or qubit. In the 4.46 T magnetic field of the trap these levels are split by approximately $\Omega_0 = 2\pi \times 124$ GHz. The $^9\text{Be}^+$ nucleus has spin $I = 3/2$. We optically pump the nuclear spin to the $m_I = +3/2$ level (*51*), where it remains throughout the duration of an experiment. The ions are Doppler laser-cooled to a temperature ~ 0.5 mK by two 313 nm laser beams tuned approximately 10 MHz below the $|\uparrow\rangle \rightarrow \left|^2P_{3/2}\, m_J = +3/2\right\rangle$ cycling transition and directed parallel and perpendicular to the magnetic field (*52*). Spins in the $|\downarrow\rangle$ state are efficiently optically pumped to the $|\uparrow\rangle$ state with a laser tuned to the $|\downarrow\rangle \rightarrow \left|^2P_{3/2}\, m_J = +1/2\right\rangle$ transition. A typical experimental cycle starts with ~ 3 ms of combined Doppler laser cooling and repumping. We estimate the fidelity of the $|\uparrow\rangle$ state preparation should be very high ($\gg 99\%$).

Low-phase noise microwave radiation from a 124 GHz source described previously in the supplementary material to (*24*) is used to globally rotate the spins, and provides an effective transverse magnetic field in the rotating frame of the qubit. The length of the time interval required to drive $|\uparrow\rangle$ to $|\downarrow\rangle$ (π-pulse) was $\sim 60\mu$s. The fidelity of a π-pulse was measured to be greater than 99.9% in a random benchmarking experiment (*27*). The spin-echo coherence duration (T_2) was measured to be ~ 10 ms with the magnet sitting on the floor, and greater than 50 ms with the magnet vibrationally isolated (*61*). All measurements were done with the magnet sitting on the floor.

At the end of an experimental sequence we turn on the Doppler cooling laser and make a projective measurement of the ion spin state through state-dependent resonance fluorescence. With the Doppler cooling laser on, an ion in the $|\uparrow\rangle$ state scatters photons while an ion in $|\downarrow\rangle$ is dark. Specifically we detected, with f/5 light collection and a photomultiplier tube (PMT), the resonance fluorescence from all the ions in a direction perpendicular to the magnetic field (the side-view). The PMT counts are integrated over time periods of typically 1 ms for measuring averages, or 15 ms for measuring standard deviation (to reduce the impact of photon shot noise). The photon detection rate varied between 1 and 2 photons per ion per ms. The variation is due to day-to-day variation in the cooling beam intensities and positions, usually changed to optimize crystal stability. Once data collection started, the photon detection rate was held constant by fixing the Doppler cooling beams' positions and stabilizing their intensities. The integrated photon count is converted to state population measurement using a frequently repeated calibration of the counts for all the spins in $|\uparrow\rangle$ and for all spins in $|\downarrow\rangle$.

Images of the ions in the rotating frame of the crystal were obtained by using an imaging

PMT (maximum processing capability $\lesssim 100\,\text{kHz}$) to record (x,y,t) for each photon (*53*). These images were used to count the number of $^9\text{Be}^+$ ions in the crystal, and were recorded either before or after long sequences of measurements. The number of $^9\text{Be}^+$ ions slowly decreases due to the formation of BeH^+ through collisions with residual H_2 in the room-temperature vacuum system. This slow change in the $^9\text{Be}^+$ ion number was tracked by monitoring the resulting slow change in the global fluorescence. Reversing the hydride-ion formation through photodissociation of BeH^+ has been demonstrated (*54*) and can be implemented in the future with a redesign of the vacuum envelope.

We employ a recently designed and fabricated Penning trap consisting of a stack of cylindrical electrodes (see sketch in Fig. 1 of the main text) to generate an electrostatic potential $q\phi_{trap}(\rho, z) \simeq \frac{1}{2}m\omega_z^2\left(z^2 - \rho^2/2\right)$ near the center of the trap, where z and ρ are cylindrical coordinates. With potentials of up to 2 kV we obtain $\omega_z \simeq 2\pi \times 1.57\,\text{MHz}$ while nulling the lowest order anharmonic (C_4) term. The direction of the magnetic field of the trap is aligned with the symmetry axis (the z-axis) of the electrodes to better than $0.01°$. The rotation frequency ω_r of the ion array determines the strength of the radial confinement of the ion crystal, and is precisely controlled by a rotating quadrupole potential (*55–57*). The middle electrode of the trap incorporates eight azimuthally segmented rotating wall electrodes at a radius of 1 cm from the center of the trap. This configuration enables control of smaller arrays than possible in our previous trap, presumably because stronger rotating wall potentials are easily generated. For most of the measurements recorded here, the rotating wall potential is characterized by $q\phi_{2,2}(x_R, y_R) = \frac{1}{2}m\omega_q^2\left(x_R^2 - y_R^2\right)$ where $\omega_q \simeq 2\pi \times (28\,\text{kHz})$ and x_R, y_R denote coordinates in the rotating frame.

Optical-Dipole Force and Lamb-Dicke Confinement

A spin-dependent optical dipole force is obtained from a moving 1D optical lattice generated at the intersection of two off-resonant laser beams. The set-up is identical to that described in (*25, 58*) and in the supplementary material to (*24*), except the beams cross with an angle $\theta = 20°$ ($\pm10°$ with respect to the central $z = 0$ plane of the trap). The optical dipole force (ODF) beams are detuned by approximately 20 GHz from any electric dipole transitions in Fig. S1 and produce an AC Stark shift on the $|\uparrow\rangle$ and $|\downarrow\rangle$ states,

$$
\begin{aligned}
\Delta_{\uparrow,acss} &= \epsilon_\uparrow + \tfrac{1}{2}U_\uparrow \sin\left[\delta\vec{k}\cdot\vec{\hat{r}} - \mu t\right] \\
\Delta_{\downarrow,acss} &= \epsilon_\downarrow + \tfrac{1}{2}U_\downarrow \sin\left[\delta\vec{k}\cdot\vec{\hat{r}} - \mu t\right]
\end{aligned}
\tag{S1}
$$

Here $\delta\vec{k}$ and μ are the wave vector and frequency difference between the ODF beams. $\left|\delta\vec{k}\right| = 2k\sin(\theta/2) = 2\pi/(0.90\,\mu\text{m})$ for $\theta = 20^o$. We adjust the polarization and frequency of the ODF laser beams so that $\epsilon_\uparrow = \epsilon_\downarrow$ and $U_\uparrow = -U_\downarrow \equiv U$, producing a spin-dependent ODF potential,

$$
\hat{H}_{ODF} = U\sum_i \sin\left[\delta\vec{k}\cdot\vec{\hat{r}}_i - \mu t\right]\hat{\sigma}_i^z .
\tag{S2}
$$

To minimize the variation of the phase of the 1D optical lattice across the ion array we align $\delta\vec{k} \parallel \hat{z}$. We do this by minimizing decoherence of the spins with $\hat{H}_{ODF}$ applied and μ tuned to a harmonic of the rotation frequency, $\mu = n\omega_r$. By comparing the $n = 2$ and $n = 1$ decoherence signals, we estimate a misalignment error $|\Delta\theta_{err}| \lesssim 0.01^o$. For $N = 200$ (largest numbers used for data collection), the array radius is $R_0 \simeq 125\,\mu\text{m}$, and the phase difference between the center and edge of the array is $\left|\delta\vec{k}\right| R_0 \tan(\Delta\theta_{err}) \lesssim 0.15$ radians $\simeq 8.5°$.

With $\delta\vec{k} \parallel \hat{z}$, Eqn. S2 only involves the axial coordinates of the ions, $\hat{H}_{ODF} = U\sum_i \sin[\delta k\,\hat{z}_i - \mu t]\,\hat{\sigma}_i^z$, where $\delta k = \left|\delta\vec{k}\right|$. In the Lamb-Dicke confinement limit ($\delta k\,z_{rms,i} \ll 1$, $z_{rms,i} \equiv \sqrt{\langle\hat{z}_i^2\rangle}$ is the root mean square (rms) axial extent of the wave function of ion i), this reduces to $\hat{H}_{ODF} \simeq F_0 \cos(\mu t) \sum_i \hat{z}_i\hat{\sigma}_i^z$ (assuming $U/\mu \ll 1$) where $F_0 \equiv U \cdot \delta k$. The spin-dependent ODF, F_0, is reduced outside of the Lamb-Dicke confinement limit by the Debye-Waller factor $DWF_i \equiv \exp\left(-\frac{1}{2}\delta k^2 z_{rms,i}^2\right)$ (59). The Ising pair-wise coupling strengths are reduced by the square of the Debye-Waller factor. The measured Ising coupling strengths, determined from mean-field spin precession measurements, were less than the calculated coupling strengths (i.e. $U \cdot \delta k$) by 10% to 25%, in rough agreement with the Debye-Waller factors estimated below. Typical values for this work are $U \simeq \hbar 2\pi \times (6.5\,\text{kHz})$ resulting in $F_0 = 30$ yN. The calculated coupling strengths are based on well known atomic physics parameters for $^9\text{Be}^+$, and calibration of the ODF laser intensity through AC Stark shift measurements for different polarizations of the ODF beams.

Measurements indicate the temperature of the axial drumhead modes is close to the Doppler cooling limit of ~ 0.5 mK (25, 58). Neglecting the Coulomb interaction between the ions, we estimate $z_{rms,i} \simeq \sqrt{\frac{\hbar}{2m\omega_z}(2\bar{n}+1)} \simeq 71$ nm, $\delta k \cdot z_{rms,i} = 0.50$, and $DWF_i \simeq 0.88$. An improved estimate of $z_{rms,i}$ is obtained by summing the contributions from all of the transverse modes m

$$z_{rms,i} = \left(\sum_m (b_{i,m})^2 \frac{\hbar}{2m\omega_m}(2\bar{n}_m+1)\right)^{1/2} \tag{S3}$$

where $\bar{n}_m \simeq k_B T/\hbar\omega_m$ and $b_{i,m}$ is the amplitude of the mth normal mode at site i. With $N = 127$, $\omega_r = 2\pi \times 180$ kHz, $\omega_z = 2\pi \times 1.575$ MHz, and $T = 0.5$ mK (typical parameters used in this work), $z_{rms,i} \simeq 77$ nm, $\delta k \cdot z_{rms,i} = 0.54$, $DWF_i \simeq 0.86$ in the center of the array, changing to $z_{rms,i} \simeq 72$, $\delta k \cdot z_{rms,i} = 0.50$, $DWF_i \simeq 0.88$ at the radial edge of the array.

In addition to reducing the average strength of the spin-dependent ODF, a non-zero Lamb-Dicke confinement parameter gives rise to fluctuations in the spin-dependent ODF from one realization of the experiment to the next (59). These fluctuations can produce fluctuations in the induced spin-spin interactions. This appears to be a challenging problem to accurately model for a many-ion array, but large numbers of ions will tend to average out the effects of thermal motional fluctuations. For our work where $\mu - \omega_z$ is small compared to $\mu - \omega_m$ for any non-COM mode m, thermal motional fluctuations give rise to fluctuations in the single-axis twisting strength produced by the spin-dependent coupling to the COM mode. We estimate fractional

fluctuations in the single-axis twisting strength to be less than 3% for $N = 100$ and $T = 0.5$ mK. Sub-Doppler cooling the axial drumhead modes can reduce $z_{rms,i}$.

Spin Variance Measurements with Different Ion Numbers

Figure S2 shows spin variance measurements, analogous to Fig 3A of the main text, with different numbers of ions. The uncertainty, one standard error σ_S, in the measured variance $(\Delta S_\psi)^2$ is calculated as $\sigma_S = (\Delta S_\psi)^2 \sqrt{2/N_{\text{trials}}}$ where N_{trials} is the number of experimental trials. Then in Fig. S2 and Fig. 3 of the main text, one standard error on the normalized variance is determined by following standard error propagation.

Sources of Noise and Decoherence

For the analysis in the main text, we account for decoherence due to spontaneous light scattering and photon shot noise. In particular we model the measured variance in the transverse spin $(\Delta S_\psi)^2$ as

$$(\Delta S_\psi)^2 = (\Delta S_\psi|_\Gamma)^2 + \frac{m}{K^2} . \tag{S4}$$

Here $(\Delta S_\psi|_\Gamma)^2$ denotes the prediction for the transverse spin variance obtained with the engineered Ising interaction in the presence of spontaneous light scattering from the ODF laser beams (*32*). The contribution of photon shot noise to the variance is $(\Delta S_{psn})^2 = m/K^2$. Here m is the mean number of photons collected in a global fluorescence measurement and K is the number of photons collected per ion in the bright state $|\uparrow\rangle$. The angle ψ, defined in the main text, denotes the angle along which the transverse spin variance is measured. In the main text, $\left(\Delta S'_\psi\right)^2 \equiv (\Delta S_\psi)^2 - (\Delta S_{psn})^2$. We separately discuss decoherence due to spontaneous emission and photon shot noise. We also discuss a few potential sources of decoherence that may be contributing to the increase in the variance of the squeezed spin quadrature observed with increasing ion number.

Spontaneous emission

The primary source of decoherence in the simulator arises from spontaneous emission from the off-resonant ODF laser beams. Decoherence due to spontaneous light scattering from an off-resonant laser beam has been carefully studied in this system (*60*). The off-diagonal elements of the density matrix for an individual spin decay exponentially with rate $\Gamma \equiv (\Gamma_{\text{el}} + \Gamma_{\text{Ram}})/2$ where Γ_{el} and Γ_{Ram} are the decoherence rates for elastic and Raman scattering, respectively. $\Gamma_{\text{Ram}} = \Gamma_{\text{ud}} + \Gamma_{\text{du}}$ where Γ_{ud} and Γ_{du} are the rates for spontaneous transitions from $|\uparrow\rangle$ to $|\downarrow\rangle$ and from $|\downarrow\rangle$ to $|\uparrow\rangle$, respectively. Reference (*60*) provides expressions for Γ_{el} and Γ_{Ram} in terms of atomic matrix elements, and laser beam polarizations and intensities. For our set-up, $\Gamma_{\text{el}} \sim 4\Gamma_{\text{Ram}}$.

4

We use the ions to measure the individual laser beam intensities (typically $\sim 0.5\,\mathrm{W/cm^2}$) through measurements of the AC Stark shift with the polarization rotated parallel to $\hat{z}$ (the magnetic field axis). We directly measure Γ by measuring the exponential decrease in $|\langle \vec{S}\rangle|$ as a function of the time interval the ODF beam(s) is (are) turned on. We use a spin-echo sequence similar to that described in (*60*) and illustrated in Fig. 1 of the main text. We observe good agreement between the calculated and measured decoherence rates with the application of a single ODF laser beam. A typical single beam decoherence rate is $\Gamma \simeq 21.5\,\mathrm{s^{-1}}$. With the 1D optical lattice and an ODF beat note μ tuned ~ 50 to $\sim 100\,\mathrm{kHz}$ above the axial COM mode, we observe exponential decay (dashed line in Fig. 2 of the main text) of the system Bloch vector at a rate $\sim 50\%$ higher than the sum of the rates from each beam. This excess decoherence rate is observed to be relatively independent of the ODF beat note μ, and is presently not understood.

For each data set, measurements of the decoherence rate with $(\mu - \omega_z) \sim 2\pi \times 50\,\mathrm{kHz}$ were used, along with the measured Ising interaction strength and the theory of (*32*), to generate $(\Delta S_\psi|_\Gamma)^2$, displayed by the solid lines in Fig. S2 and Fig. 3 of the main text. We assume the measured excess decoherence is due to an increase in Γ_{el}. More details on the theoretical modeling is given in a subsequent section. The impact of decoherence due to spontaneous light scattering can be decreased by increasing the angle θ with which the ODF beams cross.

Photon shot noise, classical detection noise

Photon shot noise contributes to the measured transverse spin variance. For a global fluorescence measurement where m photons are collected, the variance in the number of collected photons is m. We assume the same contribution of photon shot noise to the variance of a series of global fluorescence measurements where the mean number of photons collected per measurement is m. For measuring the variance of a spin component, typical detection times were 15 ms resulting in at least $K = 15$ photons collected for an ion in the bright state. For a spin state in the equatorial plane of the Bloch sphere, the mean number of photons collected is $m = \frac{N}{2}K$, so photon shot noise will contribute to $(\Delta S_\psi)^2$ at the level $\frac{m}{K^2} = \frac{N}{4}\frac{2}{K}$. Relative to projection noise $\frac{N}{4}$, photon shot noise contributes at the level of $\frac{2}{K}$, or less than 13% (-8.8 dB) for $K > 15$. For the variance measurements in Fig. 3a, 3b, and S2, the photon shot noise is subtracted from the measured spin variance. Shot noise was accounted for in the counting statistics of Fig. 4 in the main text by convolving the theoretical probability distribution with the distribution of shot noise, as discussed in more detail in a later section. The relative contribution of photon shot noise can be reduced with longer detection times. We estimate the detection time interval can be increased by an order of magnitude before optical pumping between $|\downarrow\rangle$ and $|\uparrow\rangle$ is a consideration.

Classical fluctuations in the detection laser power, frequency, and position can contribute to the measured spin variance in our global fluorescence detection. We measure this classical detection noise σ_t^2 by initializing all the ions in $|\uparrow\rangle$ (bright state) and measuring the variance in the total photon count σ_{total}^2, and then infer $\sigma_t^2 = \sigma_{total}^2 - m$. We measured σ_t^2 to be less than 30% of photon shot noise (-14 dB below projection noise). We neglect this small contribution

5

of classical detection noise relative to photon shot noise in our analysis. Specifically we do not subtract any classical detection noise.

Magnetic field fluctuations

We measure a small amount of dephasing when running the experiments described in the text in the absence of the ODF lasers. This is due to fluctuations in the homogeneous magnetic field produced by vibrations of the superconducting magnet (*27,61*). Without the ODF beams, homogeneous fluctuations produce a dephasing proportional to the square of the Bloch vector length, $N^2/4$. We write its contribution to the transverse spin variance as $(N^2/4) \Delta\phi_{rms}^2(\tau) \sin^2(\psi)$ where $\Delta\phi_{rms}^2(\tau)$ only depends on the magnetic field noise spectrum and the length τ of the experimental sequence (*62, 63*). For spin-echo sequences and magnetic field noise dominated by low frequencies (*61*), we anticipate $\Delta\phi_{rms}^2(\tau) \propto \tau^4$. Figure S3 shows dephasing measurements obtained without the ODF beams. Both τ^2 and τ^4 dependences are observed. By taking care to minimize sources of vibration in the lab, the measured $\Delta\phi_{rms}^2(\tau)$ did not significantly vary from day to day.

Dephasing is described by the Hamiltonian $B(t) \sum_i \hat{S}_i^z$ where $B(t)$ is a stochastic process. This Hamiltonian commutes with the Ising interaction (and also with the elastic Rayleigh scattering decoherence in the master equation). The impact of magnetic-field-induced dephasing can therefore be accurately modeled, and we find its contribution to be small compared to photon shot noise for both the variance measurements (Fig. 3, main text) and the histograms (Fig. 4, main text). A more complete discussion of the impact of magnetic field fluctuations is given in a later section. We note that relative to projection noise ($N/4$), the contribution of homogeneous dephasing scales as the length of the Bloch vector ($\propto N$), becoming more important for larger numbers of ions. The measured magnetic field noise can be reduced by more than a factor of 5 by vibrationally isolating the magnet.

Other potential sources of noise

We briefly discuss a few other potential sources of dephasing that do not appear to significantly contribute to the work discussed here, but could become factors, in particular if photon shot noise is reduced.

Heating of the axial COM mode during application of the spin-dependent force is a source of dephasing. Following the discussion in Ref. (*64*), we calculate the dephasing $\Delta\phi_{rms}^2(\Delta n)$ due to a stochastic increase Δn in the COM mode occupation number during the application of a spin-dependent force F_0 for a time $\tau_s = 2\pi/\delta$ where $\delta = \mu - \omega_z$. A spin echo sequence consists of two such applications, and results in twice the dephasing (in variance),

$$\frac{\Delta\phi_{rms}^2(\Delta n)}{\Delta\phi_{proj}^2} \simeq \Delta n \cdot \frac{8F_0^2 z_0^2}{\hbar^2 \delta^2} . \tag{S5}$$

Here $\Delta\phi_{proj}^2 = 1/N$ is the angle determined by the projection noise limit and $z_0 = \sqrt{\hbar/(2m\omega_z)}$. For close detunings $\delta = 2\pi \times 1\,\text{kHz}$, $\frac{2F_0 z_0}{\hbar\delta} \sim 1$, so $\Delta n \sim 1/\text{ms}$ can cause dephasing on the

order of projection noise. For trapped ions, the COM mode is typically heated by noisy electric fields. In this case, the heating rate scales linearly with N (*58*). Measurements place an upper limit on the COM mode heating rate of 1 (quanta/s)/ion. For $\tau_s = 1$ ms and $N=100$ ions, $\Delta n \leq 0.1$. Because the COM mode heating rate may scale linearly with N, this source of dephasing will likely become more important as the ion number increases. We note that photon recoil from spontaneous light scattering with the ODF beams will produce dephasing by the mechanism described above. We estimate its contribution to be small compared with the $\Delta n = 0.1$ estimate.

For small detunings δ from the COM mode, fluctuations and drifts in the axial COM mode frequency ω_z can produce spin-motion entanglement because the decoupling condition $\tau_s = 2\pi/\delta$ may no longer be satisfied. Here τ_s is the duration of a single arm period of the spin-echo sequence. Spin-motion entanglement produces dephasing, and we calculate this dephasing with Eqs. (30) and (32) of Ref. (*58*). Let $\delta\tau_s = 2\pi + \epsilon$ where ϵ is a measure of the incomplete full circle due to error in measuring ω_z. We note that a spin echo sequence suppresses the error due to a non-zero ϵ (relative to a Ramsey sequence (*65*)), and calculate a dephasing,

$$\frac{\Delta\phi_{rms}^2(\epsilon)}{\Delta\phi_{proj}^2} \simeq \frac{F_0^2 z_0^2}{\hbar^2\delta^2}\epsilon^2 \left(\epsilon + \delta t_\pi\right)^2 (2\bar{n}+1) \ . \tag{S6}$$

Here $t_\pi \simeq 60\,\mu$s is the duration of the π-pulse in the spin echo sequence. For $\delta = 2\pi \times$ (1 kHz), $F_0 \simeq 30$ yN, $\omega_z = 2\pi \times$ (1.6 MHz), $T_{COM} = 1.0$ mK ($\bar{n}_{COM} \simeq 12$), we estimate $\Delta\phi_{rms}^2(\epsilon)/\Delta\phi_{proj}^2 < 1$ requires $\epsilon < 0.3$. This places an upper limit on the uncertainty of the axial COM mode frequency of $\Delta\omega_z < 2\pi \times 50$ Hz. During data collection we checked for a shift in the COM mode frequency every 2 s, and used this information to update μ to fix $\delta = 2\pi/\tau_s$.

Theoretical Modeling of Spin-spin Interactions with Spontaneous Emission

As discussed in the earlier section on sources of noise and decoherence, spontaneous emission must be accounted for during the interaction time. Following Ref. (*60*), there are three different types of spontaneous emission processes, shown in Fig. S4. The processes with rates Γ_{ud} and Γ_{du}, which induce spontaneous transitions from $|\uparrow\rangle$ to $|\downarrow\rangle$ and from $|\downarrow\rangle$ to $|\uparrow\rangle$, respectively, arise from Raman scattering. On the other hand, Rayleigh scattering, with associated decoherence rate Γ_{el}, produces dephasing of a spin superposition state. In typical experimental realizations, $\Gamma_{ud}, \Gamma_{du} \sim 10\,\mathrm{s}^{-1}$, and $\Gamma_{el} \sim 100 - 160\,\mathrm{s}^{-1}$ including the excess decoherence discussed in the above section on spontaneous emission. The spin dynamics in this case can be modeled by a master equation in Lindblad form, and this master equation admits an exact solution, as discussed in Ref. (*32*). Using this exact solution, we compute the contrast and spin

variance expectations from the correlation functions

$$\langle \hat{\sigma}_j^+ \rangle = \frac{e^{-\Gamma t}}{2} \prod_{k \neq j} \Phi\left(J_{jk}, t\right) , \tag{S7}$$

$$\langle \hat{\sigma}_j^a \hat{\sigma}_k^b \rangle = \frac{e^{-2\Gamma t}}{4} \prod_{l \notin \{j,k\}} \Phi\left(aJ_{jl} + bJ_{kl}, t\right) , \tag{S8}$$

$$\langle \hat{\sigma}_j^a \hat{\sigma}_k^z \rangle = \frac{e^{-\Gamma t}}{2} \Psi\left(aJ_{jk}, t\right) \prod_{l \notin \{j,k\}} \Phi\left(aJ_{jl}, t\right) , \tag{S9}$$

where $a, b \in \{+, -\}$ and

$$\Phi\left(J, t\right) = e^{-\frac{(\Gamma_{\mathrm{ud}} + \Gamma_{\mathrm{du}})t}{2}} \left[\cos\left(t\sqrt{\left(2i\gamma + 2J/N\right)^2 - \Gamma_{\mathrm{ud}}\Gamma_{\mathrm{du}}}\right) \right.$$
$$\left. + \frac{\Gamma_{\mathrm{ud}} + \Gamma_{\mathrm{du}}}{2} t \operatorname{sinc}\left(t\sqrt{\left(2i\gamma + 2J/N\right)^2 - \Gamma_{\mathrm{ud}}\Gamma_{\mathrm{du}}}\right) \right] , \tag{S10}$$

$$\Psi\left(J, t\right) = e^{-\frac{(\Gamma_{\mathrm{ud}} + \Gamma_{\mathrm{du}})t}{2}} \left[i\left(2i\gamma + 2J/N\right) - 2\gamma \right] t$$
$$\times \operatorname{sinc}\left(t\sqrt{\left(2i\gamma + 2J/N\right)^2 - \Gamma_{\mathrm{ud}}\Gamma_{\mathrm{du}}}\right) . \tag{S11}$$

In these expressions, the initial state is the product state of all spins pointing along the x direction, $\gamma = \left(\Gamma_{\mathrm{ud}} - \Gamma_{\mathrm{du}}\right)/4$, and $\Gamma = \left(\Gamma_{\mathrm{ud}} + \Gamma_{\mathrm{du}} + \Gamma_{\mathrm{el}}\right)/2$. In the case that the couplings between spins are uniform, $J_{j,k} = \bar{J}$ for all j and k, these results simplify to become

$$\langle \hat{\sigma}^+ \rangle = \frac{e^{-\Gamma t}}{2} \Phi^{N-1}\left(\bar{J}, t\right) , \tag{S12}$$

$$\langle \hat{\sigma}^a \hat{\sigma}^b \rangle = \frac{e^{-2\Gamma t}}{4} \Phi^{N-2}\left((a + b)\bar{J}, t\right) , \tag{S13}$$

$$\langle \hat{\sigma}^a \hat{\sigma}^z \rangle = \frac{e^{-\Gamma t}}{2} \Psi\left(a\bar{J}, t\right) \Phi^{N-2}\left(a\bar{J}, t\right) . \tag{S14}$$

For Eqn. 7 in the main text, we use the approximation that the time is short compared to the timescale for coherent reduction of the Bloch vector ($t \lesssim \sqrt{N}/J$), and that $\Gamma_{ud}t, \Gamma_{du}t \lesssim 1$, both of which are satisfied for the experimental data in Fig. 2b of the manuscript.

Computation of the spin-spin coupling constants

We compute the ion crystal equilibrium structure and normal modes numerically following Ref. (26), where it is shown that the spin-spin coupling constants are given by

$$J_{ij} = \frac{F_0^2 N}{2\hbar M} \sum_{m=1}^{N} \frac{b_{i,m} b_{j,m}}{\mu^2 - \omega_m^2} . \tag{S15}$$

Here, ω_m and $\mathbf{b}_m$ are the frequency and amplitude of normal mode m, respectively. We find that for the experimental parameters used in this work the coupling constants are well-represented by the form $J_{j,k} \propto 1/|r_j - r_k|^\alpha$ with r_j the position of ion j and $\alpha \sim 0.02 - 0.18$. As a particular example, the spin-spin coupling constants for $N = 127$ ions, $\omega_z = 2\pi \times 1.580\,\mathrm{MHz}$, a rotating wall rotation frequency of $2\pi \times 180\,\mathrm{kHz}$ and potential chosen to match experimental mode spectra, and a force and detuning chosen such that $\bar{J}/h = 3.30\,\mathrm{kHz}$ are shown in Fig. S5. A best fit to the computed spin-spin couplings gives a power law $\alpha \sim 0.05$.

Validation of the uniform coupling approximation

Here, we show that the uniform coupling approximation Eqs. (S12)-(S14) used in the main text is a good approximation to the solutions computed using Eqs. (S7)-(S9), with the spin-spin couplings directly determined from the phonon modes Eqn. (S15). We compare the two for the parameters of Fig. S5. The decoherence rates are taken to match measured rates of $\Gamma_{\mathrm{el}} = 171.6\mathrm{s}^{-1}$, $\Gamma_{\mathrm{ud}} = 9.2\mathrm{s}^{-1}$, $\Gamma_{\mathrm{du}} = 6.5\mathrm{s}^{-1}$. The normalized contrast and spin noise variance are compared in Fig. S6(a)-(b) and very little difference is observed. These comparisons validate the use of the uniform coupling approximation.

Computation of the Full Counting Statistics

While a computation of the full counting statistics for general spin-spin couplings J_{jk} is exponentially difficult in the number of ions, the computation can be performed efficiently with the uniform coupling approximation, $J_{jk} = \bar{J}$. Rather than directly computing the probability distribution to measure n spins along $\hat{S}^\psi = \cos\psi \hat{S}^z + \sin\psi \hat{S}^y$, $P_\psi(n)$, it is advantageous to compute the characteristic function

$$C_\psi(q) = \langle e^{iq \sum_{j=1}^N \hat{\sigma}_j^\psi} \rangle. \tag{S16}$$

From the characteristic function, the probability distribution is obtained by Fourier transformation as

$$P_\psi(n) = \frac{1}{N+1} \sum_{k=0}^N e^{-i\frac{\pi k}{N+1}n} C_\psi\left(\frac{\pi k}{N+1}\right). \tag{S17}$$

Because the spin operators $\hat{\sigma}_j^\psi$ in Eqn. (S16) mutually commute, we can write the characteristic function as

$$C_\psi(q) = \langle \prod_{j=1}^N \left[\cos(q)\hat{I}_j + i\sin(q)\hat{\sigma}_j^\psi\right] \rangle, \tag{S18}$$

where $\hat{I}_j$ is the identity operator for spin j. In the uniform coupling approximation, this becomes

$$C_\psi(q) = \langle \left(\cos(q)\hat{I} + i\sin(q)\hat{\sigma}^\psi\right)^N \rangle, \tag{S19}$$

where it is understood that multiple instances of $\hat{\sigma}^\psi$ are interpreted to correspond to operators on different spins. This result can be expanded using the binomial theorem as

$$C_\psi (q) = \sum_{n=0}^{N} \binom{N}{n} \cos^{N-n} (q) \, (i \sin (q))^n \, \langle \hat{\sigma}^\psi_{(n)} \rangle , \tag{S20}$$

where $\langle \hat{\sigma}^\psi_{(n)} \rangle$ denotes the expectation with n $\hat{\sigma}^\psi$ operators on different spins, e.g., $\langle \hat{\sigma}^\psi_{(2)} \rangle = \langle \hat{\sigma}^\psi_1 \hat{\sigma}^\psi_2 \rangle$. In the uniform coupling approximation, validated in Fig. S6, the system is permutationally symmetric and so $\langle \hat{\sigma}^\psi_i \hat{\sigma}^\psi_j \rangle = \langle \hat{\sigma}^\psi_{(2)} \rangle$ for all $i \neq j$. Expanding a product of n $\hat{\sigma}^\psi$ in terms of n_+ $\hat{\sigma}^+$s, n_- $\hat{\sigma}^-$s, and $(n - n_+ - n_-) \, \hat{\sigma}^z$s, the final result for the characteristic function in the uniform coupling approximation is

$$
\begin{aligned}
\langle C_\psi (q) \rangle = {} & \sum_{n=0}^{N} \binom{N}{n} \cos^{N-n} (q) \, (i \sin (q))^n \\
& \times \sum_{n_+=0}^{n} \sum_{n_-=0}^{n-n_+} \frac{n!}{n_+! n_-! (n - n_+ - n_-)!} (-i \sin \psi)^{n_+} (i \sin \psi)^{n_-} \\
& \times (\cos \psi)^{n - n_+ - n_-} \, \langle \hat{\sigma}^+_{(n_+)} \hat{\sigma}^-_{(n_-)} \hat{\sigma}^z_{(n-n_+-n_-)} \rangle .
\end{aligned}
\tag{S21}
$$

Using the methods of Ref. (*32*), we can write the correlation function as

$$
\begin{aligned}
\langle \hat{\sigma}^+_{(n_+)} \hat{\sigma}^-_{(n_-)} \hat{\sigma}^z_{(n_z)} \rangle = {} & \frac{e^{-(n_+ + n_-)\Gamma t}}{2^{n_+ + n_-}} \Psi^{n_z} \left((n_+ - n_-) J, t \right) \\
& \times \Phi^{N-(n_+ + n_- + n_z)} \left((n_+ - n_-) J, t \right) ,
\end{aligned}
\tag{S22}
$$

which leads to a fully analytic representation of the counting statistics. A comparison of the counting statistics with and without the effects of decoherence from spontaneous emission for the parameters of Fig. S6 is given in Fig. S7. The quadrature for $\hat{S}^\psi$ at $\psi = 88°$, which is characteristic of antisqueezing, is more strongly affected by decoherence than the quadrature along the squeezed direction, $\psi = 174.6°$. The fast oscillations exhibited by the Hamiltonian evolution are washed out by decoherence.

Theoretical modeling of magnetic field fluctuations and photon shot noise

As mentioned in an earlier section, homogenous fluctuations in the magnetic field caused by vibrations of the magnet contribute to dephasing. In the absence of decoherence, the effect of a time-fluctuating, homogeneous magnetic field with Hamiltonian $\hat{H}_B = B(t) \sum_i \hat{S}^z_i$ on an arbitrary permutation-symmetric correlation function is

$$\langle \hat{\sigma}^+_{(n_+)} \hat{\sigma}^-_{(n_-)} \hat{\sigma}^z_{(n_z)} \rangle_B = e^{i\varphi(\tau)(n_+ - n_-)} \langle \hat{\sigma}^+_{(n_+)} \hat{\sigma}^-_{(n_-)} \hat{\sigma}^z_{(n_z)} \rangle_{B \to 0} , \tag{S23}$$

where $\varphi\left(\tau\right) = \int_0^{\tau/2} dt\, B\left(t\right) - \int_{\tau/2}^\tau dt\, B\left(t\right)$ for the spin-echo sequence used in the experiment. While this expression is no longer exact in the presence of Raman decoherence, it is an excellent approximation in the experimentally relevant case that $B\left(t\right)$ is small and elastic decoherence dominates over Raman decoherence. Averaging over realizations of the fluctuating field $\varphi\left(\tau\right)$, we find

$$\overline{e^{i\varphi(\tau)(n_+ - n_-)}} = 1 - \frac{(n_+ - n_-)^2}{2}\Delta\phi_{rms}^2\left(\tau\right) + \ldots$$

$$= e^{-\frac{(n_+ - n_-)^2}{2}\Delta\phi_{rms}^2(\tau)}, \tag{S24}$$

where the overbar denotes averaging of the stochastic variable, $\Delta\phi_{rms}^2\left(\tau\right) = \overline{\varphi^2\left(\tau\right)}$, and we have used the fact that $\overline{\varphi\left(\tau\right)} = 0$. The variance $\Delta\phi_{rms}^2\left(\tau\right)$ is determined experimentally, as shown in Fig. S3. With this, we find that the correlation functions in the presence of a fluctuating magnetic field are obtained as

$$\overline{\langle \hat{\sigma}_{(n_+)}^+ \hat{\sigma}_{(n_-)}^- \hat{\sigma}_{(n_z)}^z \rangle_B} \tag{S25}$$

$$\approx e^{-\frac{(n_+ - n_-)^2 \Delta\phi_{rms}^2(\tau)}{2}} \langle \hat{\sigma}_{(n_+)}^+ \hat{\sigma}_{(n_-)}^- \hat{\sigma}_{(n_z)}^z \rangle_{B \to 0}.$$

A comparison of the experimentally measured counting statistics with no ODF beams ($\bar{J}$ and all decoherence rates set to zero) with the theory that models magnetic field noise with Eqn. (S25) is shown in Fig. S8, demonstrating that the noise is accounted for consistently. In particular, we see that the dependence on tomography angle ψ of the variance due to magnetic field noise is accurately captured. In Fig. S9, we show the difference between the theoretical predictions for the counting statistics with and without homogeneous magnetic field noise, using the parameters of Fig. S6, a total interaction time of $\tau = 3$ms, and $\Delta\phi_{rms}^2\left(\tau\right) = 0.035$. We see that the magnetic field noise has a relatively slight effect on the full counting statistics. This can be understood by noting that the correlations which are significantly affected by the magnetic field noise (those with $(n_+ - n_-) \neq 0$) are already suppressed by the factor $e^{-(n_+ + n_-)\Gamma t}$ due to decoherence from spontaneous emission. The final source of noise we include in our theoretical predictions is photon shot noise, which is accounted for by convolving the theoretical counting statistics P_ψ with the distribution of photon shot noise P_{psn}. For the present case, the distribution of shot noise is taken to be Gaussian with standard deviation 0.03 in units of $S_\psi/(N/2)$ (11% of spin projection noise). A comparison of the results with and without this convolution is given in Fig. S10. Also, we note that the dashed lines in Fig. S10, which include all the sources of noise described above, are plotted in Fig. 4 of the main text with a different normalization. In order to compare the discrete probability distribution which does not include shot noise with the continuous distribution resulting from the convolution, the latter is evaluated on the set of points where the former has support and normalized so that its sum is unity.

Extraction of the Fisher information from the Hellinger distance

The Fisher information F, which measures the distinguishability of quantum states with respect to small phase rotations, is a many-particle entanglement witness, with a measurement of $F/N > n$ implying that the state is n-particle entangled. Importantly, this characterization of entanglement holds even for non-Gaussian states, where spin squeezing is no longer an effective witness. Further, the bound $F/N > 1$ is both a necessary and sufficient condition for the ability to perform sub-shot-noise phase estimation with a quantum state (*45*).

We characterize the Fisher information following the method of Ref. (*40*), which utilizes the Euclidean distance in the space of probability amplitudes known as the (squared) Hellinger distance,

$$d_H^2 \left(\theta \right) = \frac{1}{2} \sum_n \left(\sqrt{P_\theta \left(n \right)} - \sqrt{P_0 \left(n \right)} \right)^2 . \tag{S26}$$

Here, $P_0 \left(n \right)$ denotes the counting statistics along the optimal tomography angle ψ, $P_\theta \left(n \right)$ denotes the counting statistics after rotation by θ around y, and $\sum_n$ denotes the metric such that $\sum_n P_\theta \left(n \right) = 1$. As shown in Ref. (*40*), for small angles θ, the squared Hellinger distance satisfies

$$d_H^2 \left(\theta \right) = \frac{F}{8} \theta^2 + \mathcal{O} \left(\theta^3 \right) . \tag{S27}$$

We use a quartic fit to the squared Hellinger distance for small rotation angles to extract the quadratic coefficient, and from this the Fisher information per particle. In the absence of photon shot noise, but including the decoherence from spontaneous emission and magnetic field noise, we find $F/N = 2.1$, while including photon shot noise drops this value to $F/N = 0.57$, as shown in Fig. 4C of the main text. This comparison demonstrates that the experiment generates an over-squeezed state consistent with entanglement, but that this entanglement cannot be experimentally verified with the present magnitude of photon shot noise. In Fig.4C of the main text, we also showed a determination of the Fisher information in the absence of noise or decoherence of any kind, in which case $F/N = 34.4$.

To further emphasize the consistency between theory and experiment, in Fig. S11 we compare the theoretically predicted and experimentally measured Fisher information for a squeezed state of 50 ions, with $\xi_R^2 = 0.42$ (-3.8 dB). The experimentally observed Fisher information per ion, with no noise subtractions or corrections, is $F/N = 2.6(2)$, in agreement with the theory prediction of $F/N = 2.8$.
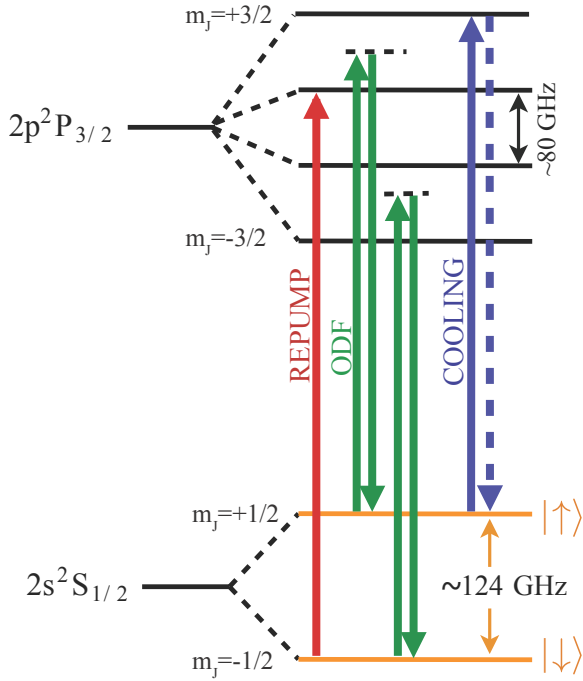
Figure S1: Relevant energy levels of $^9\text{Be}^+$ at $B_0 = 4.46$ T (not drawn to scale). We only show $m_I = +\frac{3}{2}$ levels which are prepared experimentally through optical pumping. The $^2S_{1/2} - {}^2P_{3/2}$ transition wavelength is 313 nm. A resonant laser beam provides Doppler laser cooling and state discrimination, a second repumps $|\downarrow\rangle$ to the $|\uparrow\rangle$. The ODF interaction is due to a pair of beams (derived from the same laser) with relative detuning μ. The qubit splitting $\Omega_0 \sim 2\pi \times 124$ GHz. A low phase noise microwave source at Ω_0 provides full global control over spins.
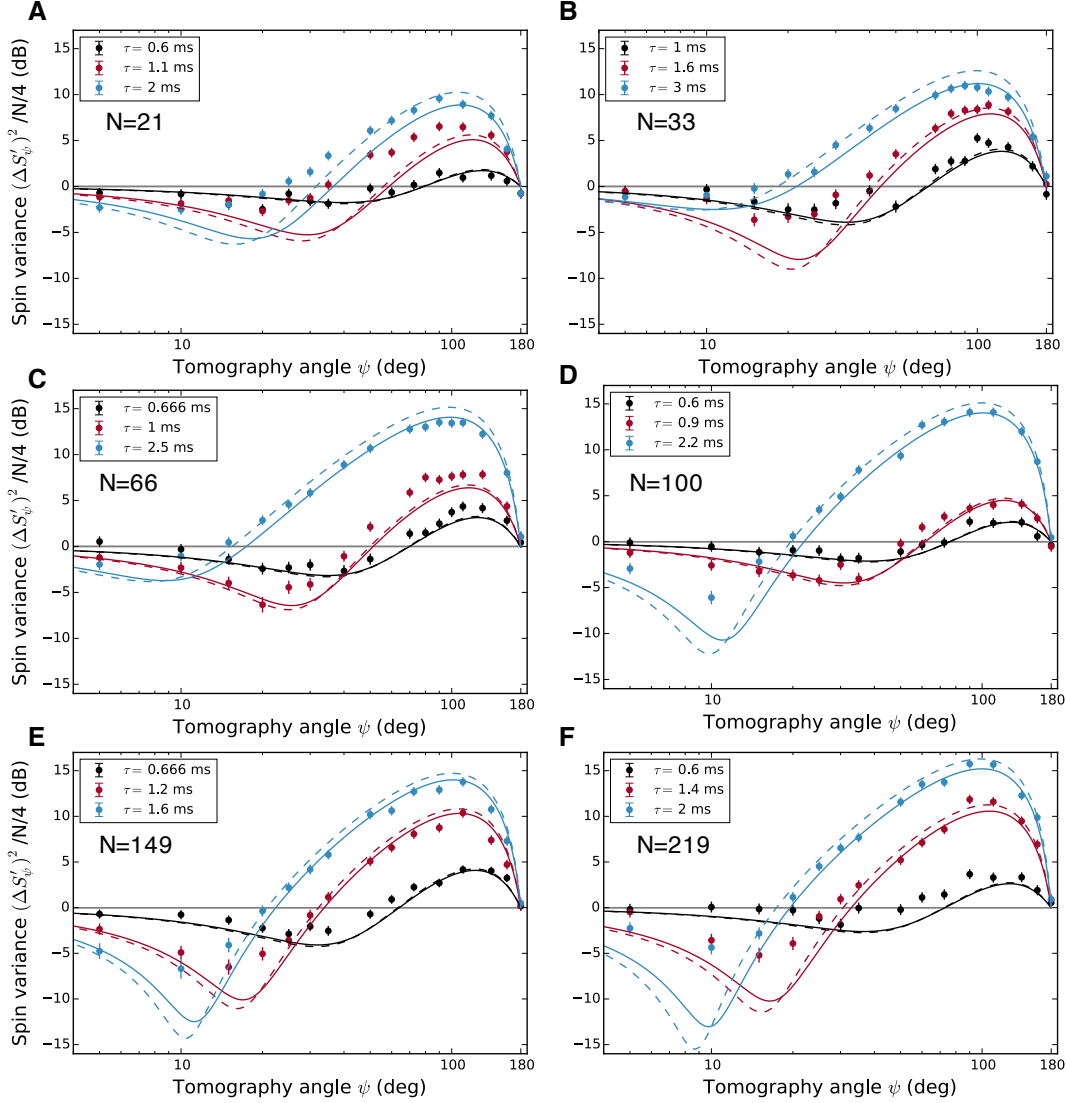
Figure S2: Spin variance as a function of tomography angle ψ for different ion numbers N, calculated from $N_{\text{trials}} = 200$ trials. The error bars are one standard error on the variance. The solid lines are a prediction, with no free parameters, assuming homogenous Ising interactions and including decoherence from spontaneous emission. The dashed lines are a theoretical prediction with the same interaction parameters but no decoherence.
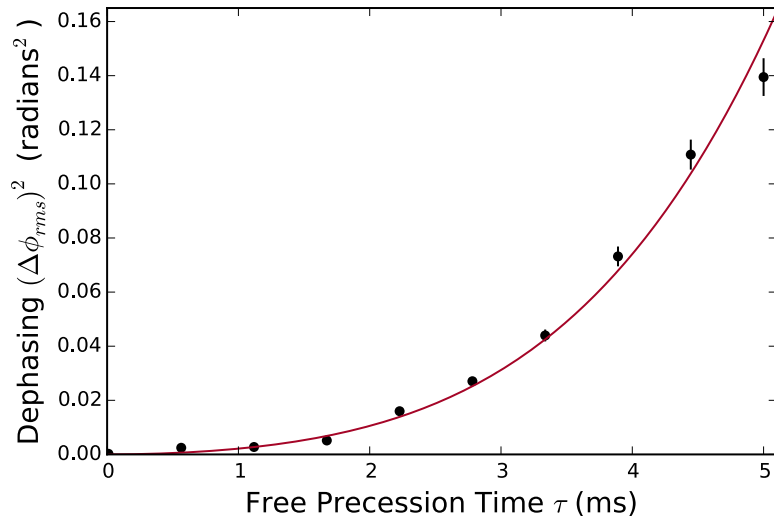
Figure S3: Dephasing due to magnetic field fluctuations measured with $N = 124(3)$ ions in the absence of the ODF beams. Plotted is the variance of the dephasing angle $\Delta\phi(\tau)$ determined from 300 trials of a spin echo experiment measuring the transverse spin noise along $\psi = 90°$. Photon shot noise was subtracted; τ is the sum of the two free precession intervals. The red line is a 2-parameter fit $\Delta\phi^2_{rms}(\tau) = (2.4 \times 10^{-3}/\text{ms}^2)\,\tau^2 + (1.7 \times 10^{-4}/\text{ms}^4)\,\tau^4$ where τ is in ms.
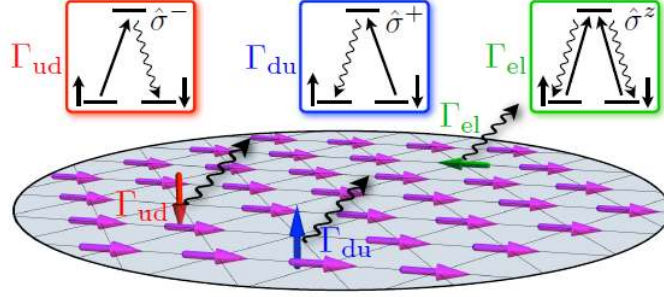
Figure S4: Spontaneous emission from the Raman beams creating the spin-dependent force causes three types of decoherence: Raman decoherence processes with rates Γ_{ud} and Γ_{du}, which project spins to be down or up, respectively, and elastic decoherence processes, which cause dephasing of a spin superposition state. Figure from Ref. (*32*).
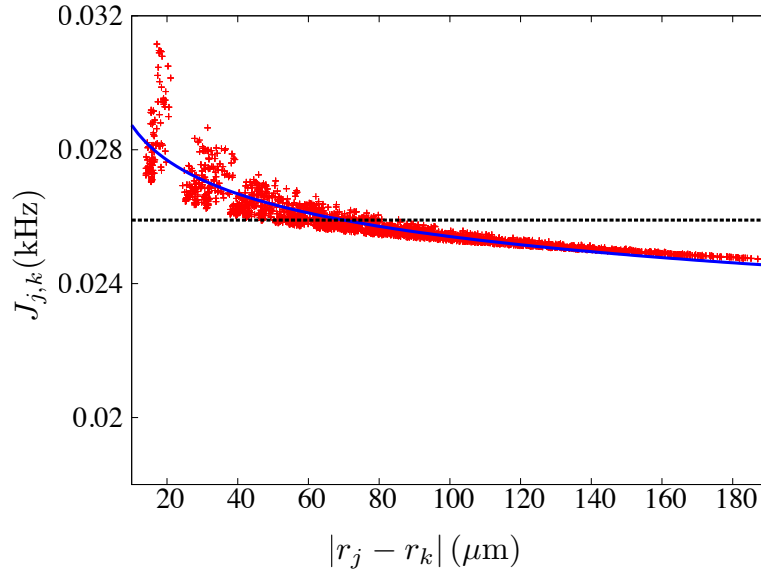
Figure S5: Spin-spin couplings for the experimental parameters given in the main text (red points), together with their best power-law fit $\alpha \sim 0.05$ (blue solid line) and the uniform coupling approximation (black dashed line).
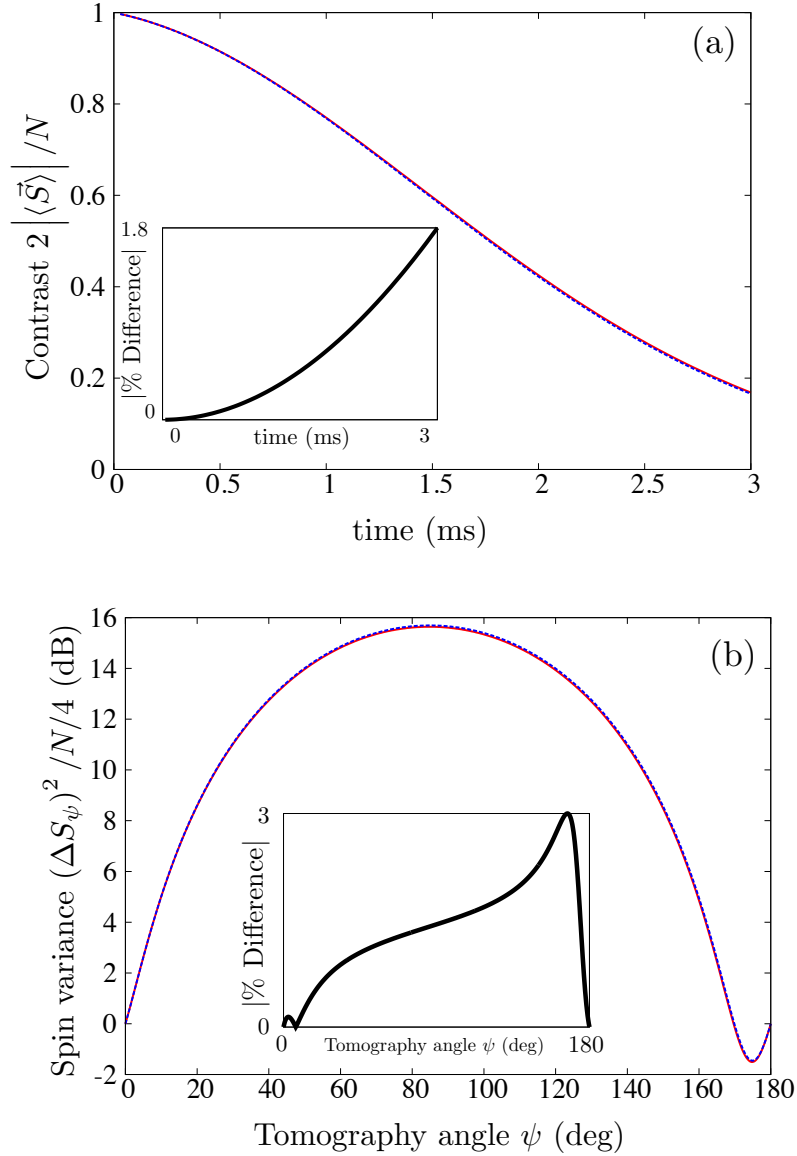
Figure S6: Normalized contrast (panel (a)) and spin noise variance (panel (b)) computed using Eqs. (S7)-(S9) (solid red lines) and the uniform coupling approximation Eqs. (S12)-(S14) (dashed blue lines) for the spin-spin couplings of Fig. S5. The insets show the percent difference between the results. The parameters used are $N = 127$, $\bar{J}/h = 3.30\,\text{kHz}$, $\Gamma_{\text{el}} = 171.6\text{s}^{-1}$, $\Gamma_{\text{ud}} = 9.2\text{s}^{-1}$, $\Gamma_{\text{du}} = 6.5\text{s}^{-1}$, and an interaction time of 3ms in panel (b).
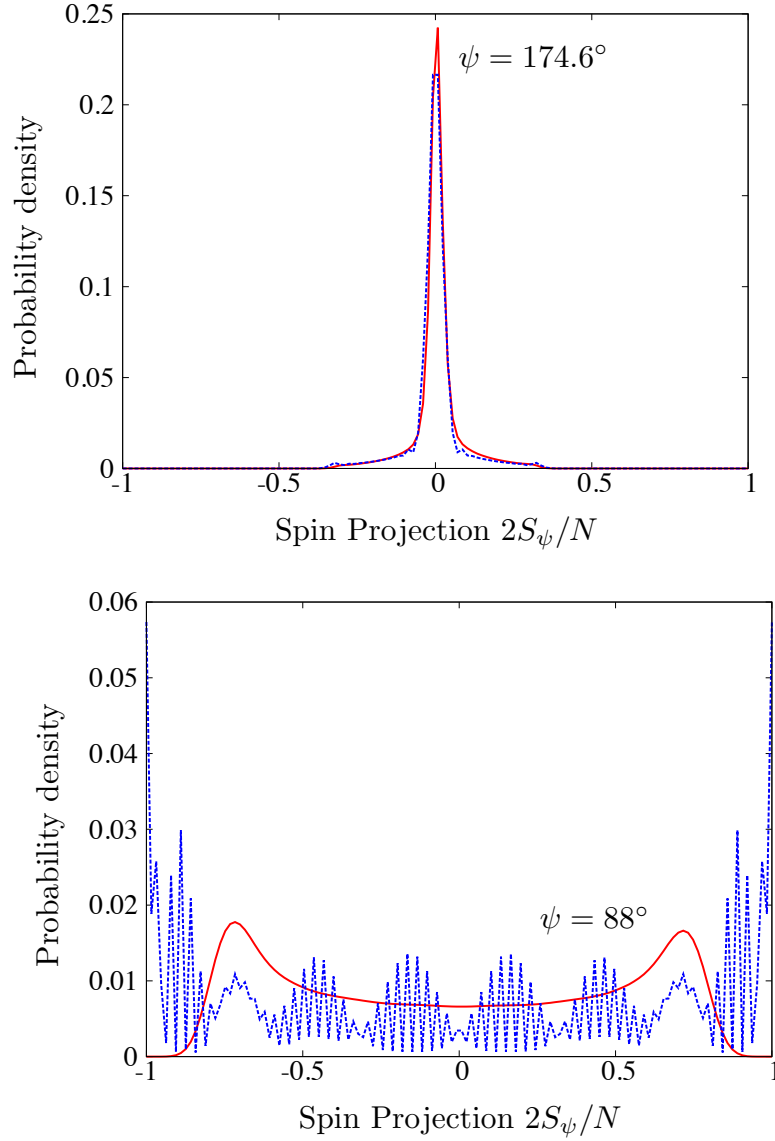
Figure S7: Full counting statistics with (red solid) and without (blue dashed) decoherence from spontaneous emission for the squeezed (upper panel, $\psi = 174.6°$) and anti-squeezed (lower panel, $\psi = 88°$) quadratures. Decoherence more significantly affects the anti-squeezed quadrature.
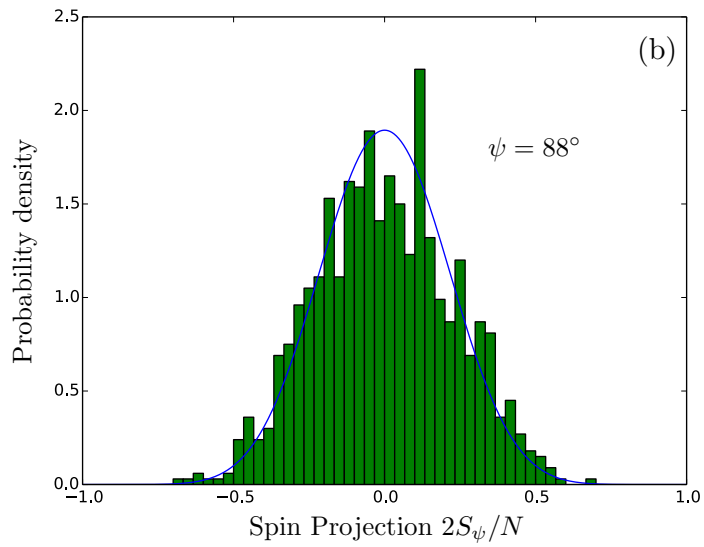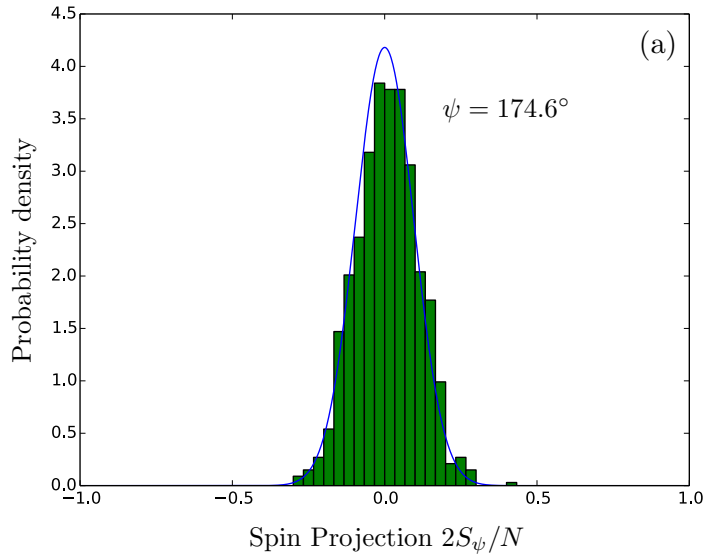
Figure S8: Experimentally measured histogram of counting statistics in the absence of ODF beams (bars) compared with the theoretical prediction (solid line) including magnetic field and photon shot noise. The upper panel is for the squeezed quadrature $\psi = 174.6°$, while the lower panel is for the anti-squeezed quadrature $\psi = 88°$.
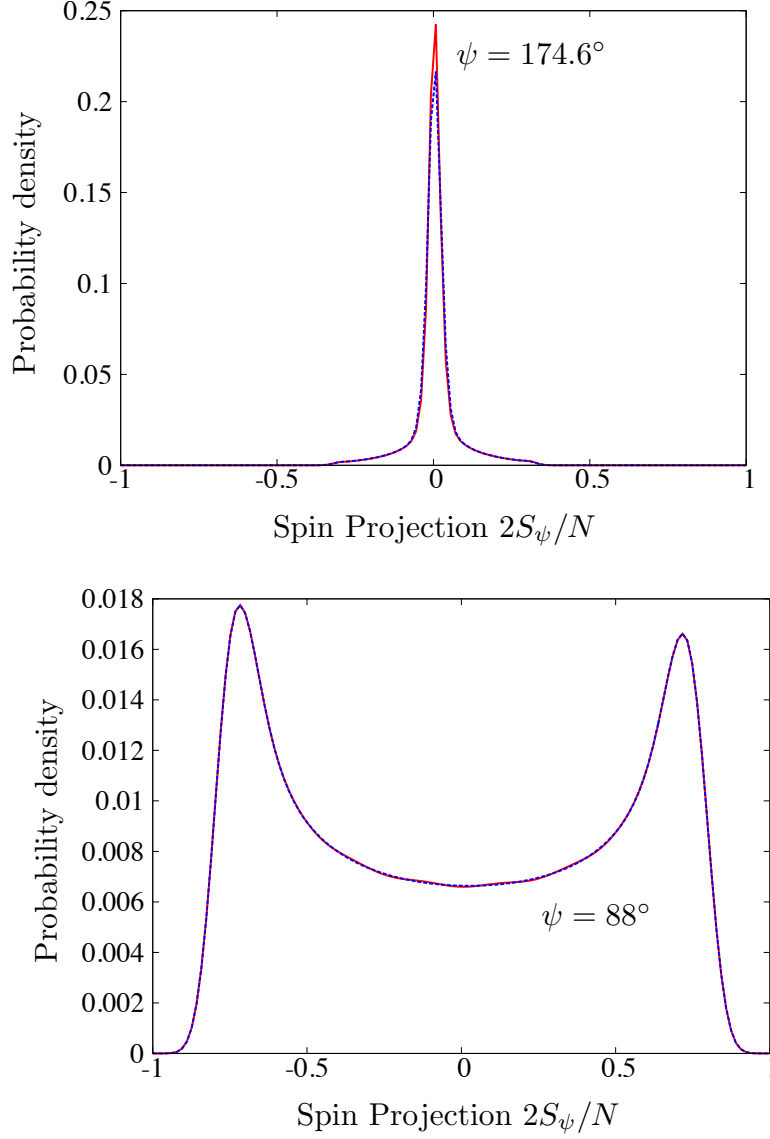
Figure S9: Full counting statistics without (red solid) and with (blue dashed) homogeneous magnetic field noise for the squeezed (upper panel, $\psi = 174.6°$) and anti-squeezed (lower panel, $\psi = 88°$) quadratures. The effects of magnetic field noise are strongly suppressed by decoherence. The asymmetry in the peaks at positive and negative S_ψ are due to unequal Raman decoherence rates $\Gamma_{\mathrm{du}} \neq \Gamma_{\mathrm{ud}}$.
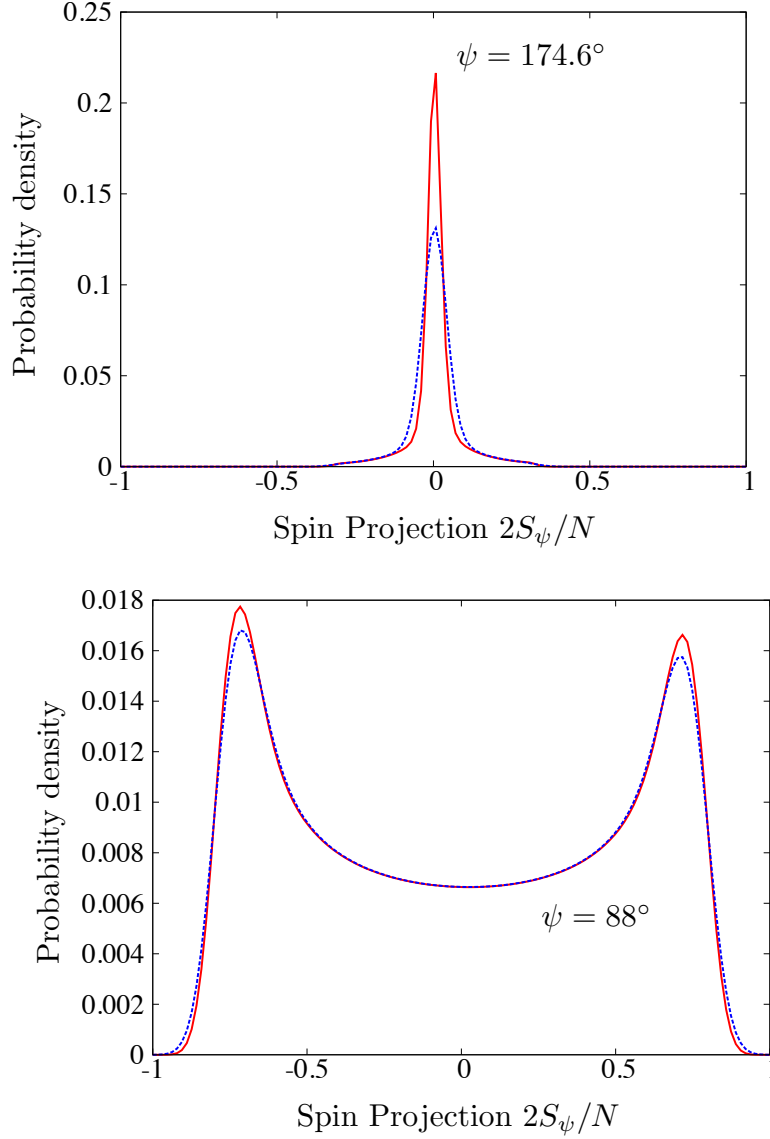
Figure S10: Full counting statistics without (red solid) and with (blue dashed) convolution with photon shot noise. Both curves also include homogeneous magnetic field noise. The upper panel is for the squeezed quadrature $\psi = 174.6°$, while the lower panel is for the anti-squeezed quadrature $\psi = 88°$. In order to compare the discrete distribution without shot noise to the continuous distribution with shot noise, the latter was evaluated on the support of the former and normalized to sum to 1. Note that the normalization of the data is different than in Fig. 4 of the main text, but the blue lines are otherwise identical.
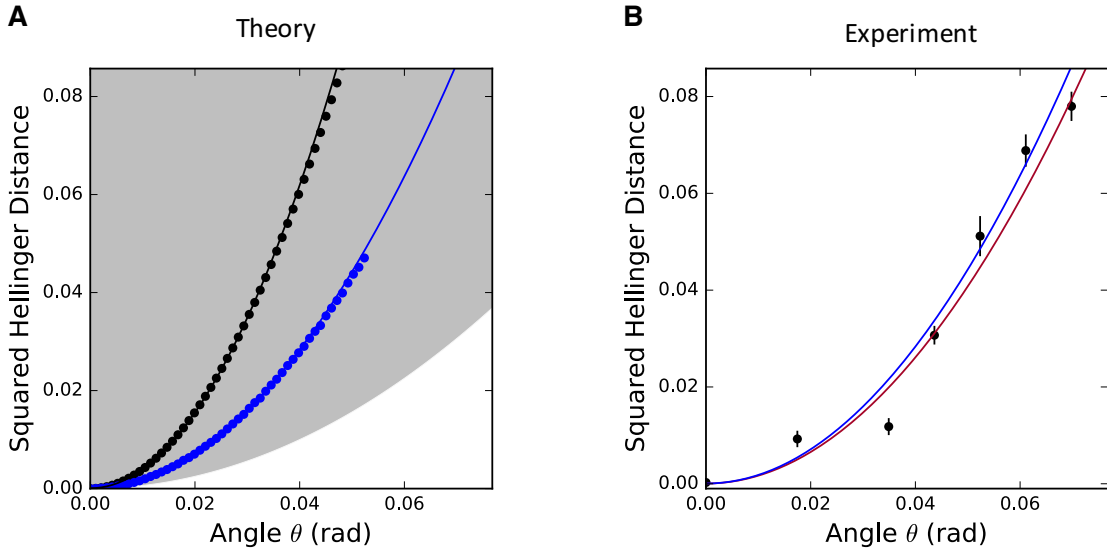
Figure S11: **Fisher information for a squeezed state of 50 ions.** The state analyzed here is formed from an interaction time $\tau = 1$ ms, with $\bar{J} = 1990$, and $\psi = 15°$. **(A)** Extraction of the Fisher information from the theoretically computed Hellinger distance without (black) and with (blue) photon shot noise, including the effects of decoherence from spontaneous emission and magnetic field noise. The points denote computed values of the Hellinger distance and the lines are small-angle quadratic fits used to extract the Fisher information. The gray swath denotes the region of entangled states. **(B)** Extraction of the Fisher information from the experimentally measured Hellinger distance, using a quadratic fit (red line). The Hellinger distance is computed from histograms of repeated trials of the experiment (black points). The reference histogram at $\theta = 0$ is formed from 2100 trials, and the other histograms are formed from 700 trials. In both the theory and experiment, the histogram bin size is one spin, which is slightly above the detection resolution for this data set.

References

1. R. P. Feynman, Simulating physics with computers. *Int. J. Theor. Phys.* **21**, 467–488 (1982). doi:10.1007/BF02650179

2. P. Hauke, F. M. Cucchietti, L. Tagliacozzo, I. Deutsch, M. Lewenstein, Can one trust quantum simulators? *Rep. Prog. Phys.* **75**, 082401 (2012). Medline doi:10.1088/0034-4885/75/8/082401

3. I. M. Georgescu, S. Ashhab, F. Nori, Quantum simulation. *Rev. Mod. Phys.* **86**, 153–185 (2014). doi:10.1103/RevModPhys.86.153

4. R. J. Elliott, P. Pfeuty, C. Wood, Ising model with a transverse field. *Phys. Rev. Lett.* **25**, 443–446 (1970). doi:10.1103/PhysRevLett.25.443

5. K. Binder, A. P. Young, Spin glasses: Experimental facts, theoretical concepts, and open questions. *Rev. Mod. Phys.* **58**, 801–976 (1986). doi:10.1103/RevModPhys.58.801

6. R. Nandkishore, D. A. Huse, Many-body localization and thermalization in quantum statistical mechanics. *Annu. Rev. Condens. Matter Phys.* **6**, 15–38 (2015). doi:10.1146/annurev-conmatphys-031214-014726

7. D. Belitz, T. R. Kirkpatrick, T. Vojta, How generic scale invariance influences quantum and classical phase transitions. *Rev. Mod. Phys.* **77**, 579–632 (2005). doi:10.1103/RevModPhys.77.579

8. S. Sachdev, *Quantum Phase Transitions* (Wiley, 2007).

9. T. F. Rønnow, Z. Wang, J. Job, S. Boixo, S. V. Isakov, D. Wecker, J. M. Martinis, D. A. Lidar, M. Troyer, Defining and detecting quantum speedup. *Science* **345**, 420–424 (2014). Medline doi:10.1126/science.1252319

10. A. Lucas, Ising formulations of many NP problems. *Front. Phys.* **2**, 5 (2014). doi:10.3389/fphy.2014.00005

11. J. Simon, W. S. Bakr, R. Ma, M. E. Tai, P. M. Preiss, M. Greiner, Quantum simulation of antiferromagnetic spin chains in an optical lattice. *Nature* **472**, 307–312 (2011). Medline doi:10.1038/nature09994

12. A. de Paz, A. Sharma, A. Chotia, E. Maréchal, J. H. Huckans, P. Pedri, L. Santos, O. Gorceix, L. Vernac, B. Laburthe-Tolra, Nonequilibrium quantum magnetism in a dipolar lattice gas. *Phys. Rev. Lett.* **111**, 185305 (2013). Medline doi:10.1103/PhysRevLett.111.185305

13. T. Fukuhara, S. Hild, J. Zeiher, P. Schauß, I. Bloch, M. Endres, C. Gross, Spatially resolved detection of a spin-entanglement wave in a Bose-Hubbard chain. *Phys. Rev. Lett.* **115**, 035302 (2015). Medline doi:10.1103/PhysRevLett.115.035302

14. R. C. Brown, R. Wyllie, S. B. Koller, E. A. Goldschmidt, M. Foss-Feig, J. V. Porto, Two-dimensional superexchange-mediated magnetization dynamics in an optical lattice. *Science* **348**, 540–544 (2015). Medline doi:10.1126/science.aaa1385

15. I. D. Leroux, M. H. Schleier-Smith, V. Vuletić, Implementation of cavity squeezing of a collective atomic spin. *Phys. Rev. Lett.* **104**, 073602 (2010). Medline doi:10.1103/PhysRevLett.104.073602

16. B. Yan, S. A. Moses, B. Gadway, J. P. Covey, K. R. Hazzard, A. M. Rey, D. S. Jin, J. Ye, Observation of dipolar spin-exchange interactions with lattice-confined polar molecules. *Nature* **501**, 521–525 (2013). Medline doi:10.1038/nature12483

17. D. Porras, J. I. Cirac, Effective quantum spin systems with trapped ions. *Phys. Rev. Lett.* **92**, 207901 (2004). Medline doi:10.1103/PhysRevLett.92.207901

18. P. Jurcevic, B. P. Lanyon, P. Hauke, C. Hempel, P. Zoller, R. Blatt, C. F. Roos, Quasiparticle engineering and entanglement propagation in a quantum many-body system. *Nature* **511**, 202–205 (2014). Medline doi:10.1038/nature13461

19. P. Richerme, Z. X. Gong, A. Lee, C. Senko, J. Smith, M. Foss-Feig, S. Michalakis, A. V. Gorshkov, C. Monroe, Non-local propagation of correlations in quantum systems with long-range interactions. *Nature* **511**, 198–201 (2014). Medline doi:10.1038/nature13450

20. R. Islam, C. Senko, W. C. Campbell, S. Korenblit, J. Smith, A. Lee, E. E. Edwards, C. C. Wang, J. K. Freericks, C. Monroe, Emergence and frustration of magnetism with variable-range interactions in a quantum simulator. *Science* **340**, 583–587 (2013). Medline doi:10.1126/science.1232296

21. R. Schmied, J. H. Wesenberg, D. Leibfried, Optimal surface-electrode trap lattices for quantum simulation with trapped ions. *Phys. Rev. Lett.* **102**, 233002 (2009). Medline doi:10.1103/PhysRevLett.102.233002

22. C. D. Bruzewicz, R. McConnell, J. Chiaverini, J. M. Sage, http://arxiv.org/abs/1511.03293 (2015).

23. J. D. Baltrusch, A. Negretti, J. M. Taylor, T. Calarco, Fast and robust quantum computation with ionic Wigner crystals. *Phys. Rev. A* **83**, 042319 (2011). doi:10.1103/PhysRevA.83.042319

24. J. W. Britton, B. C. Sawyer, A. C. Keith, C. C. Wang, J. K. Freericks, H. Uys, M. J. Biercuk, J. J. Bollinger, Engineered two-dimensional Ising interactions in a trapped-ion quantum simulator with hundreds of spins. *Nature* **484**, 489–492 (2012). Medline doi:10.1038/nature10981

25. B. C. Sawyer, J. W. Britton, A. C. Keith, C. C. Wang, J. K. Freericks, H. Uys, M. J. Biercuk, J. J. Bollinger, Spectroscopy and thermometry of drumhead modes in a mesoscopic trapped-ion crystal using entanglement. *Phys. Rev. Lett.* **108**, 213003 (2012). Medline doi:10.1103/PhysRevLett.108.213003

26. C.-C. J. Wang, A. C. Keith, J. K. Freericks, Phonon-mediated quantum spin simulator employing a planar ionic crystal in a Penning trap. *Phys. Rev. A* **87**, 013422 (2013). doi:10.1103/PhysRevA.87.013422

27. M. J. Biercuk, H. Uys, A. P. Vandevender, N. Shiga, W. M. Itano, J. J. Bollinger, High-fidelity quantum control using ion crystals in a penning trap. *Quantum Inf. Comput.* **9**, 920–949 (2009).

28. See supplementary materials on *Science* Online.

29. D. Leibfried, B. DeMarco, V. Meyer, D. Lucas, M. Barrett, J. Britton, W. M. Itano, B. Jelenković, C. Langer, T. Rosenband, D. J. Wineland, Experimental demonstration of a robust, high-fidelity geometric two ion-qubit phase gate. *Nature* **422**, 412–415 (2003). Medline doi:10.1038/nature01492

30. M. Kastner, Diverging equilibration times in long-range quantum spin models. *Phys. Rev. Lett.* **106**, 130601 (2011). doi:10.1103/PhysRevLett.106.130601

31. M. V. D. Worm, B. C. Sawyer, J. J. Bollinger, M. Kastner, Relaxation timescales and decay of correlations in a long-range interacting quantum simulator. *New J. Phys.* **15**, 083007 (2013). [doi:10.1088/1367-2630/15/8/083007](doi:10.1088/1367-2630/15/8/083007)

32. M. Foss-Feig, K. R. A. Hazzard, J. J. Bollinger, A. M. Rey, Nonequilibrium dynamics of arbitrary-range Ising models with decoherence: An exact analytic solution. *Phys. Rev. A* **87**, 042101 (2013). doi:10.1103/PhysRevA.87.042101

33. K. R. A. Hazzard, M. van den Worm, M. Foss-Feig, S. R. Manmana, E. G. Dalla Torre, T. Pfau, M. Kastner, A. M. Rey, Quantum correlations and entanglement in far-from-equilibrium spin systems. *Phys. Rev. A* **90**, 063622 (2014). doi:10.1103/PhysRevA.90.063622

34. D. Wineland, J. Bollinger, W. Itano, F. Moore, D. J. Heinzen, Spin squeezing and reduced quantum noise in spectroscopy. *Phys. Rev. A* **46**, R6797 (1992). doi:10.1103/PhysRevA.46.R6797

35. A. Sørensen, L. M. Duan, J. I. Cirac, P. Zoller, Many-particle entanglement with Bose-Einstein condensates. *Nature* **409**, 63–66 (2001). Medline [doi:10.1038/35051038](doi:10.1038/35051038)

36. L. K. Shalm, R. B. A. Adamson, A. M. Steinberg, Squeezing and over-squeezing of triphotons. *Nature* **457**, 67–70 (2009). Medline doi:10.1038/nature07624

37. W. Wasilewski, K. Jensen, H. Krauter, J. J. Renema, M. V. Balabas, E. S. Polzik, Quantum noise limited and entanglement-assisted magnetometry. *Phys. Rev. Lett.* **104**, 133601 (2010). Medline doi:10.1103/PhysRevLett.104.133601

38. C. D. Hamley, C. S. Gerving, T. M. Hoang, E. M. Bookjans, M. S. Chapman, Spin-nematic squeezed vacuum in a quantum gas. *Nat. Phys.* **8**, 305–308 (2012). doi:10.1038/nphys2245

39. C. F. Ockeloen, R. Schmied, M. F. Riedel, P. Treutlein, Quantum metrology with a scanning probe atom interferometer. *Phys. Rev. Lett.* **111**, 143001 (2013). Medline doi:10.1103/PhysRevLett.111.143001

40. H. Strobel, W. Muessel, D. Linnemann, T. Zibold, D. B. Hume, L. Pezzè, A. Smerzi, M. K. Oberthaler, Fisher information and entanglement of non-Gaussian spin states. *Science* **345**, 424–427 (2014). Medline doi:10.1126/science.1250147

41. N. Behbood, F. Martin Ciurana, G. Colangelo, M. Napolitano, G. Tóth, R. J. Sewell, M. W. Mitchell, Generation of macroscopic singlet states in a cold atomic ensemble. *Phys. Rev. Lett.* **113**, 093601 (2014). doi:10.1103/PhysRevLett.113.093601

42. O. Hosten, N. J. Engelsen, R. Krishnakumar, M. A. Kasevich, Measurement noise 100 times lower than the quantum-projection limit using entangled atoms. *Nature* **529**, 505–508 (2016). Medline doi:10.1038/nature16176

43. K. C. Cox, G. P. Greve, J. M. Weiner, J. K. Thompson, Deterministic squeezed states with collective measurements and feedback. *Phys. Rev. Lett.* **116**, 093602 (2016). Medline doi:10.1103/PhysRevLett.116.093602

44. M. Kitagawa, M. Ueda, Squeezed spin states. *Phys. Rev. A* **47**, 5138–5143 (1993). Medline doi:10.1103/PhysRevA.47.5138

45. L. Pezzé, A. Smerzi, Entanglement, nonlinear dynamics, and the Heisenberg limit. *Phys. Rev. Lett.* **102**, 100401 (2009). Medline doi:10.1103/PhysRevLett.102.100401

46. J. Smith *et al.*, http://arxiv.org/abs/1508.07026 (2015).

47. K. Arnold, E. Hajiyev, E. Paez, C. H. Lee, M. D. Barrett, J. Bollinger, Prospects for atomic clocks based on large ion crystals. *Phys. Rev. A* **92**, 032108 (2015). doi:10.1103/PhysRevA.92.032108

48. B. Lücke, J. Peise, G. Vitagliano, J. Arlt, L. Santos, G. Tóth, C. Klempt, Detecting multiparticle entanglement of Dicke states. *Phys. Rev. Lett.* **112**, 155304 (2014). Medline doi:10.1103/PhysRevLett.112.155304

49. F. Haas, J. Volz, R. Gehr, J. Reichel, J. Estève, Entangled states of more than 40 atoms in an optical fiber cavity. *Science* **344**, 180–183 (2014). Medline doi:10.1126/science.1248905

50. R. McConnell, H. Zhang, J. Hu, S. Ćuk, V. Vuletić, Entanglement with negative Wigner function of almost 3,000 atoms heralded by one photon. *Nature* **519**, 439–442 (2015). Medline doi:10.1038/nature14293

51. W. M. Itano, D. J. Wineland, Precision measurement of the ground-state hyperfine constant of ^{25}Mg$^+$. *Phys. Rev. A* **24**, 1364–1373 (1981). doi:10.1103/PhysRevA.24.1364

52. M. J. Jensen, T. Hasegawa, J. J. Bollinger, Temperature and heating rate of ion crystals in Penning traps. *Phys. Rev. A* **70**, 033401 (2004). doi:10.1103/PhysRevA.70.033401

53. T. B. Mitchell, J. J. Bollinger, W. M. Itano, D. H. E. Dubin, Stick-slip dynamics of a stressed ion crystal. *Phys. Rev. Lett.* **87**, 183001 (2001). doi:10.1103/PhysRevLett.87.183001

54. B. C. Sawyer, J. G. Bohnet, J. W. Britton, J. J. Bollinger, Reversing hydride-ion formation in quantum-information experiments with Be^+. *Phys. Rev. A* **91**, 011401 (2015). doi:10.1103/PhysRevA.91.011401

55. X.-P. Huang, J. J. Bollinger, T. B. Mitchell, W. M. Itano, D. H. E. Dubin, Precise control of the global rotation of strongly coupled ion plasmas in a Penning trap. *Phys. Plasmas* **5**, 1656 (1998). doi:10.1063/1.872834

56. D. H. E. Dubin, T. M. O'Neil, Trapped nonneutral plasmas, liquids, and crystals (the thermal equilibrium states). *Rev. Mod. Phys.* **71**, 87–172 (1999). doi:10.1103/RevModPhys.71.87

57. T. Hasegawa, M. J. Jensen, J. J. Bollinger, Stability of a Penning trap with a quadrupole rotating electric field. *Phys. Rev. A* **71**, 023406 (2005). doi:10.1103/PhysRevA.71.023406

58. B. C. Sawyer, J. W. Britton, J. J. Bollinger, Spin dephasing as a probe of mode temperature, motional state distributions, and heating rates in a two-dimensional ion crystal. *Phys. Rev. A* **89**, 033408 (2014). doi:10.1103/PhysRevA.89.033408

59. D. J. Wineland, C. Monroe, W. M. Itano, D. Leibfried, B. E. King, D. M. Meekhof, Experimental issues in coherent quantum-state manipulation of trapped atomic ions. *J. Res. Natl. Inst. Stand. Technol.* **103**, 259 (1998). doi:10.6028/jres.103.019

60. H. Uys, M. J. Biercuk, A. P. Vandevender, C. Ospelkaus, D. Meiser, R. Ozeri, J. J. Bollinger, Decoherence due to elastic Rayleigh scattering. *Phys. Rev. Lett.* **105**, 200401 (2010). Medline doi:10.1103/PhysRevLett.105.200401

61. J. W. Britton *et al*., https://arxiv.org/abs/1512.00801 (2015).

62. M. J. Biercuk, H. Uys, A. P. VanDevender, N. Shiga, W. M. Itano, J. J. Bollinger, Optimized dynamical decoupling in a model quantum memory. *Nature* **458**, 996–1000 (2009). Medline doi:10.1038/nature07951

63. Ł. Cywiński, R. M. Lutchyn, C. P. Nave, S. Das Sarma, How to enhance dephasing time in superconducting qubits. *Phys. Rev. B* **77**, 174509 (2008). doi:10.1103/PhysRevB.77.174509

64. R. Ozeri, W. M. Itano, R. B. Blakestad, J. Britton, J. Chiaverini, J. D. Jost, C. Langer, D. Leibfried, R. Reichle, S. Seidelin, J. H. Wesenberg, D. J. Wineland, Errors in trapped-ion quantum gates due to spontaneous photon scattering. *Phys. Rev. A* **75**, 042329 (2007). doi:10.1103/PhysRevA.75.042329

65. D. Hayes, S. M. Clark, S. Debnath, D. Hucul, I. V. Inlek, K. W. Lee, Q. Quraishi, C. Monroe, Coherent error suppression in multiqubit entangling gates. *Phys. Rev. Lett.* **109**, 020503 (2012). doi:10.1103/PhysRevLett.109.020503